Geochemistry Geophysics Geosystems G3

AN ELECTRONIC JOURNAL OF THE EARTH SCIENCES

Published by AGU and the Geochemical Society

Article

Volume 6, Number 7

12 July 2005

Q07002, doi:10.1029/2004GC000900

ISSN: 1525-2027

Cooling rate effects on paleointensity estimates in submarine basaltic glass and implications for dating young flows

Julie Bowles and Jeffrey S. Gee

Scripps Institution of Oceanography, University of California, San Diego, 9500 Gilman Drive, MC 0220, La Jolla, California 92093, USA (jbowles@ucsd.edu)

Dennis V. Kent

Department of Geology, Rutgers University, 610 Taylor Road, Piscataway, New Jersey 08854, USA

Lamont-Doherty Earth Observatory, Columbia University, 61 Route 9W, P.O. Box 1000, Palisades, New York 10964-8000, USA

Eric Bergmanis and John Sinton

Department of Geology and Geophysics, University of Hawaii, 1680 East-West Road, Honolulu, Hawaii 96822, USA

[1] Cooling rate effects on the intensity of thermoremanent magnetization (TRM) have been well documented in ceramics. In that case, laboratory cooling is generally more rapid than the initial cooling, leading to an overestimate of the paleofield by 5–10% in Thellier-type paleointensity experiments. The reverse scenario, however, has never been tested. We examine the effects of cooling rate on paleointensity estimates from rapidly quenched submarine basaltic glass (SBG) samples from 13 sites at 17°30′–18°30′S on the East Pacific Rise. Absolute cooling rates determined by relaxation geospeedometry at five of these sites range from ~10 to ~330°C min^{-1} at the glass transition (~650°C). Over the dominant range of remanence blocking temperatures (~200–400°C), the natural cooling rates are approximately equal to or slightly slower than the laboratory cooling rates during the Thellier experiment. These results suggest that while the cooling rate effect might introduce some within-site scatter, it should not result in a systematic bias in paleointensity from SBG. Paleointensity estimates from the 15 sites range from ~29 to 59 μT, with an average standard error of ~1 μT. Comparison with models of geomagnetic field intensity variations at the site indicate the youngest group of samples is very recent (indistinguishable from present-day) and the oldest is at least 500, and probably several thousand, years old. These age estimates are consistent with available radiometric ages and geologic observations.

Components: 13,198 words, 12 figures, 4 tables.

Keywords: East Pacific Rise; geomagnetic paleointensity; paleomagnetic dating; relaxation geospeedometry; submarine basaltic glass.

Index Terms: 1521 Geomagnetism and Paleomagnetism: Paleointensity; 1527 Geomagnetism and Paleomagnetism: Paleomagnetism applied to geologic processes; 8416 Volcanology: Mid-oceanic ridge processes (1032, 3614).

Received 16 December 2004; **Revised** 14 April 2005; **Accepted** 29 April 2005; **Published** 12 July 2005.

Bowles, J., J. S. Gee, D. V. Kent, E. Bergmanis, and J. Sinton (2005), Cooling rate effects on paleointensity estimates in submarine basaltic glass and implications for dating young flows, *Geochem. Geophys. Geosyst.*, *6*, Q07002, doi:10.1029/2004GC000900.

1. Introduction

[2] The effect of cooling rate on the intensity of thermoremanent magnetization (TRM) has been well documented in ceramics, with slower cooling resulting in higher magnetization. The theoretical magnitude of the effect in single domain magnetite is ~3–7% change in magnetization per order of magnitude change in cooling rate [*Halgedahl et al.*, 1980; *Dodson and McClelland-Brown*, 1980; *Walton*, 1980]. This has important implications for Thellier-type paleointensity experiments where the ratio of a laboratory TRM to the natural remanent magnetization (NRM) is used to infer the intensity of the field when the sample originally cooled. If a sample cooled slower in nature than it did in the laboratory, the ancient field intensity will be overestimated.

[3] The effect of cooling rate is readily verified experimentally in archeomagnetic materials that often cool over hours to days in kilns, but cool in 20–30 minutes in a typical Thellier experiment. Theory would predict that a paleointensity derived from this ceramic will overestimate the true field value by 5–13%. *Genevey and Gallet* [2002] carried out controlled experiments on ceramic samples with either pseudo-single domain magnetite, or a combination of magnetite and hematite. They found that for an original cooling time of 33 hours (versus a laboratory cooling time of 0.5 hr), paleointensity is overestimated on average by ~10%, but the effect spanned a wide range (~3–20%). *Fox and Aitken* [1980] similarly found a 2–9% overestimation for samples cooled over 120 minutes versus 5 minutes, and a 7–14% overestimation for cooling over 960 minutes versus 5 minutes. Similar direct tests of the theory on intrusive rocks cooling over thousands to millions of years are impossible, but theory predicts paleofield estimates in such samples will overestimate the true field by up to ~50% [*Selkin et al.*, 2000; *Halgedahl et al.*, 1980]. Clearly, careful studies of paleointensity must take cooling rate into account when natural cooling rates differ significantly from laboratory conditions.

[4] Cooling rate effects have not been considered at the other end of the cooling rate spectrum, however. Is it possible to underestimate the field with samples that cooled quicker in nature than possible than in the laboratory? Although most geologic materials will have cooling rates comparable to or slower than laboratory rates (~10^1–10^2 °C min^{-1}), rapidly cooled volcanic material may exceed laboratory cooling rates. For example, *Wallace et al.* [2003] used a water speciation geospeedometer to estimate cooling rates as high as 10^3 °C min^{-1} (range 10^{-2} to 10^3 °C min^{-1}) in Plinian-fall and pyroclastic flow deposits of the Bishop Tuff.

[5] In this paper we specifically address the effect of cooling rate on paleofield estimates from submarine basaltic glass (SBG). Quenched in 2°C water, one might expect that these samples cool quicker in nature than under laboratory conditions, leading to an underestimate of paleointensity. *Wilding et al.* [2000] used relaxation geospeedometry to find cooling rates ranging from 25 to 0.15°C min^{-1} in hyaloclastites from a seamount on the flanks of the East Pacific Rise, approximately equal to or slower than our estimated laboratory rates. However, they also calculated that within 2.5 mm of the rock/water interface glass should cool at rates up to 3500°C min^{-1} (at the glass transition, here ~600°C). If we accept that these calculations are valid in at least some cases, then the combined calculated and experimentally determined rates span five orders of magnitude, approximately centered on the laboratory cooling rate.

[6] Documenting cooling rates in SBG is particularly important given recent suggestions [*Carlut and Kent*, 2000; *Gee et al.*, 2000; *Carlut et al.*, 2004] that paleointensity estimates might be used, in conjunction with geomagnetic field models [e.g., *Jackson et al.*, 2000], to determine eruptive ages for very young mid-ocean ridge lavas. In particular, the range of possible cooling rates in SBG indicates that (1) a paleointensity estimate could be biased high OR low by ~10% and (2) within-site scatter could be significant for this application.

[7] In this paper we test the theory that cooling-rate variation in paleointensity is observable in SBG. We carry out Thellier-type paleointensity experiments on a set of SBG from 17°–18°S on the East Pacific Rise. We then apply a relaxation geospeedometry technique to estimate the original cooling rate of the samples. By comparing within-site variation in cooling rate with variation in paleointensity, we address the question of a correlation between the two and the implications for paleointensity estimates and dating of flows through paleointensity.

2. Geologic Background

[8] We chose five samples from 17°30′–18°30′S on the East Pacific Rise (Figure 1) for both

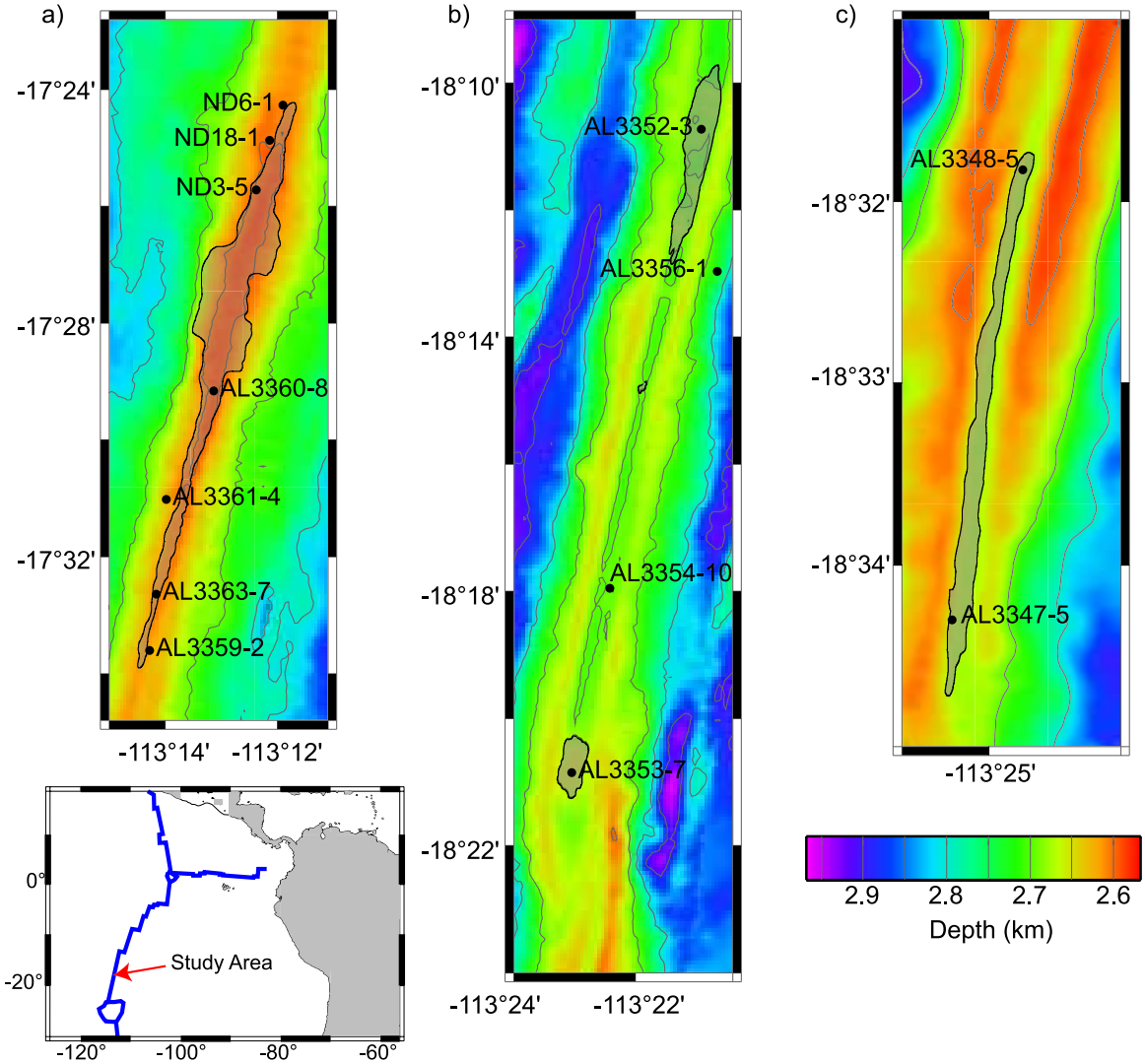

Figure 1. Sample location map. Shaded areas with heavy black outlines represent boundaries of relatively young lava flows as used by *Sinton et al.* [2002]: (a) Aldo Kihi flow field; (b) Moai (north) and Lava Shield (south) flows; (c) South Hump lava. The 100 m contours are shown in gray.

paleointensity and cooling rate analysis. An additional eight samples were only subjected to paleointensity analysis. Table 1 lists sample locations, depths and location descriptions. Samples were collected either with the *Nautile* submersible during the 1993 Nautile Dorsale Ultra-Rapide (NAUDUR) cruise [*Auzende et al.*, 1996] or with the *Alvin* submersible during the 1999 STOWA cruise [*Sinton et al.*, 2002]. Characterized by rapid spreading rates (~145 mm/yr [*Naar and Hey*, 1989]), the axis along this segment has a shallow (<2590 m) dome-shaped axial high near 17°30′S which transitions into a graben structure to the south [*Sinton et al.*, 2002]. The samples were collected near the summit of the axial high or within the graben where there was little to no sediment cover in a region with a high sedimentation rate (2–30 cm/kyr [*Sinton et al.*, 2002, and references therein]).

[9] Three samples (ND3-5, AL3360-8, AL3363-7) were taken from the Aldo-Kihi flow field at ~17°30′S (Figure 1a). This lava field consists of multiple individual flows (primarily lobate) that have been mapped for 18.5 km along axis and cover 14 km^2. The flows have little to no sediment cover and are thought to have been at least partially erupted in the late 1980s to early 1990s, although there is some evidence that it was not erupted in a single event [*Sinton et al.*, 2002]. On the basis of submersible observations of sediment cover and superposition, sample ND6-1, collected north of

Table 1. Samples Selected for Analysis[a]

Sample	Lat, S	Lon, W	Depth, m	Description	Experiment
			Northern Area (Figure 1a)		
ND3-5	17°25.72′	113°12.38′	2571	Aldo-Kihi flow	P, C
AL3360-8	17°29.13′	113°13.13′	2572	Aldo-Kihi flow	P, C
AL3363-7	17°32.63′	113°14.15′	2592	Aldo-Kihi flow	P, C
ND6-1	17°24.27′	113°11.90′	2590	northwest of Aldo-Kihi flow	P, C
ND18-1	17°24.90′	113°12.12′	2578	Rehu Marka flow (NW of Aldo-Kihi)	P
AL3361-4	17°31.10′	113°13.97′	2589	west of Aldo-Kihi flow	P, C
AL3359-2	17°33.60′	113°14.29′	2598	southeast of Aldo-Kihi flow	P, C
			Middle Area (Figure 1b)		
AL3352-3	18°10.72′	113°20.90′	2668	Moai flow	P
AL3356-1	18°12.96′	113°20.55′	2758	relatively older flow; outside graben	P, C
AL3354-10	18°17.94′	113°22.44′	2677	relatively older flow; inside graben	P
AL3353-7	18°20.88′	113°23.04′	2637	Lava Shield	P
			Southern Area (Figure 1c)		
AL3348-5	18°31.86′	113°24.78′	2611	northern South Hump	P
AL3347-5	18°34.32′	113°25.20′	2651	southern South Hump	P

[a] Note that sample prefix ND indicates it was sampled with *Nautile* during the NAUDUR cruise; AL indicates sampling by *Alvin* during the STOWA cruise. P, paleointensity; C, cooling rate. See *Sinton et al.* [2002] for further descriptions.

Aldo Kihi, and sample AL3359-2, collected to the south, appear to be just slightly older than the Aldo Kihi flow. ND18-1 was taken from the Rehu Marka flow, to the northwest of Aldo Kihi and AL3361-4 was sampled just west of the Aldo Kihi flow, about 550 m from the ridge axis. On the basis of the geologic evidence, these latter two samples are older than both Aldo Kihi and samples ND6-1 and AL3359-2; observations of sediment cover suggest that AL3361-4 is older than ND18-1.

[10] Four samples were collected close to the axial summit near 18°S (Figure 1b), an area characterized by older, intensely tectonized flows with significant sediment cover. Sample AL3354-10 was taken from inside the axial summit graben, and AL3356-1 was collected on the eastern flank of the EPR about 1 km from the axis. Obviously younger, untectonized flows have been erupted in places within the graben, and samples AL3352-3 and AL3353-7 were collected from the younger Moai flow and Lava Shield, respectively [*Sinton et al.*, 2002].

[11] The final two samples were taken from the South Hump area (Figure 1c), where a relatively young flow fills the graben at 18°30′S. AL3348-5, taken from the northern South Hump, and AL3347-5, from the southern South Hump, have distinctly different chemical compositions, and are separated by a vertical offset in the imaged axial magma chamber (AMC) reflector [*Sinton et al.*, 2002]. However, there is no geological evidence for a flow boundary between the northern and southern South Hump lavas.

3. Paleointensity and Rock Magnetic Analysis

3.1. Techniques

[12] Five to nine individual unoriented specimens of fresh glass (0.11–1.29 g) were selected from each site for paleointensity analysis. Most glass was vesicle-free with small to moderate (~10%) amounts of plagioclase phenocrysts. In addition to unoriented samples, several large pieces of glass up to ~2 cm thick showed a small amount of orange/brown hydrothermal precipitate on the surface that allowed orientation with respect to the water-rock interface. To the extent that this precipitate reflects the original cooling interface, one might expect to see a correlation in cooling rate versus distance from interface, and possibly a corresponding correlation in paleointensity. To evaluate any such systematic variations, these pieces (one each from sites AL3363-7 and AL3359-2, and two from AL3361-4) were mounted in wax and ~4 mm slices were taken roughly parallel to the presumed rock-water interface.

[13] In every case, the samples from the outermost slice had very weak magnetic moments ($<5 \times 10^{-10}$ Am^2). These samples either had insufficient moment to obtain a reliable measure-

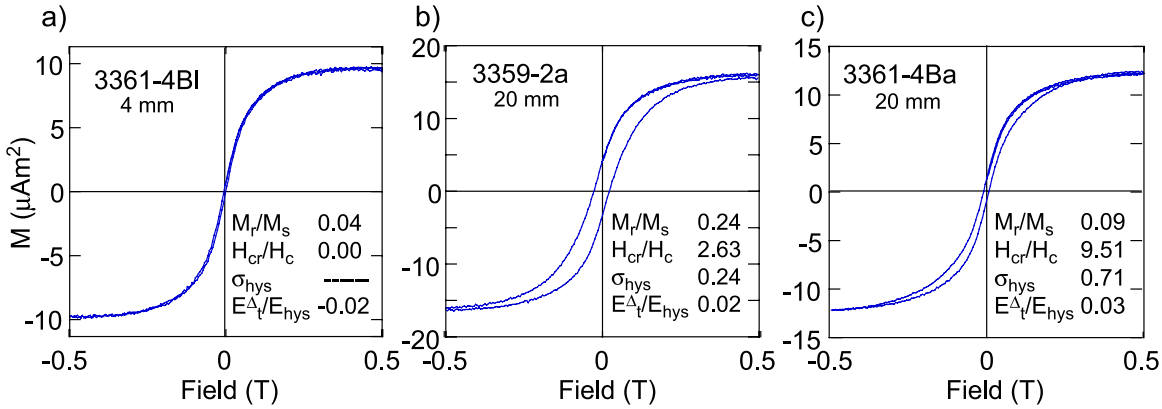

Figure 2. Slope-corrected hysteresis loops and parameters for selected samples. Distance from inferred water-rock interface is shown in mm. Samples closest to interface show SP behavior, while samples farthest from interface consistently show SD-SP behavior. Maximum field applied was 1 T (only shown to 0.5 T).

ment or were likely to become too weak during the course of the Thellier experiment. Samples ~8–12 mm from the inferred water-rock interface usually had sufficiently high moments for the paleointensity experiment, and 1–3 samples from each of the remaining slices were chosen for analysis.

[14] All samples selected for the paleointensity experiments were soaked in a dilute (15%) HCl solution to remove any superficial staining. Samples were then packed into glass tubes (1 cm diameter by 3 cm long) with glass microfiber filter paper, and were fixed in place with several drops of potassium silicate. Fiducial lines were etched into the tubes to ensure constant orientation throughout the experiment.

[15] We used the stepwise double-heating method of *Thellier and Thellier* [1959], modified by *Coe* [1967], to recover an estimate of the ancient field. We used an applied field of 40 μT, which varied by <0.5% inside the sample chamber. Samples were heated at 100, 150, and 200°C, then at 25°C intervals until the zero-field magnetization intensity was ≤10% of the natural remanent magnetization (NRM). The maximum temperature to which the samples were subjected ranged from 350–525°C. The temperature varied by no more than 6°C from one end of the sample chamber to the other, and temperature reproducibility is significantly better than that [*Selkin et al.*, 2000]. Thermal alteration of the sample was monitored by pTRM checks (repeating a lower temperature pTRM) after every other temperature step.

[16] In addition to the paleointensity experiments, we carried out hysteresis measurements on several (unheated) chips of glass to constrain magnetic grain size. Samples were taken from both the outer-most and inner-most (with respect to the water-rock interface) portions of two of the oriented samples (AL3361-4B, and AL3359-2). In addition to the standard hysteresis curve, we also measured the "saturation initial curve" to measure the transient energy dissipation [*Fabian*, 2003], or transient hysteresis [*Yu and Tauxe*, 2005].

3.2. Results

[17] Clean hysteresis curves were difficult to obtain because the signal was dominated by a large paramagnetic contribution. However, hysteresis results from the samples closest to the water-rock interface generally display typical superparamagnetic (SP)-type curves (Figure 2a), consistent with the extremely low NRM of these samples. Samples farthest from the water-rock interface (20 mm) display a "wasp-waisted" constriction, typical of a mixture of single domain (SD) and SP grains (Figures 2b and 2c). To quantify this constriction, we calculated the shape parameter (σ_{hys}) and transient energy dissipation ratio ($E_{t\Delta}/E_{hys}$) of *Fabian* [2003]. σ_{hys} compares the area of the hysteresis curve to that of an ideal rectangle. Values >0 are reflective of a constricted curve, and increasing σ_{hys} suggests an increasing SP contribution (or an independent mineral fraction). We calculated values significantly >0 for samples at 20 mm depth. Also, $E_{t\Delta}/E_{hys}$, the ratio of irreversible to reversible self-demagnetization, is negligible for all of these samples, indicating an SD-SP mixture. Taken to-

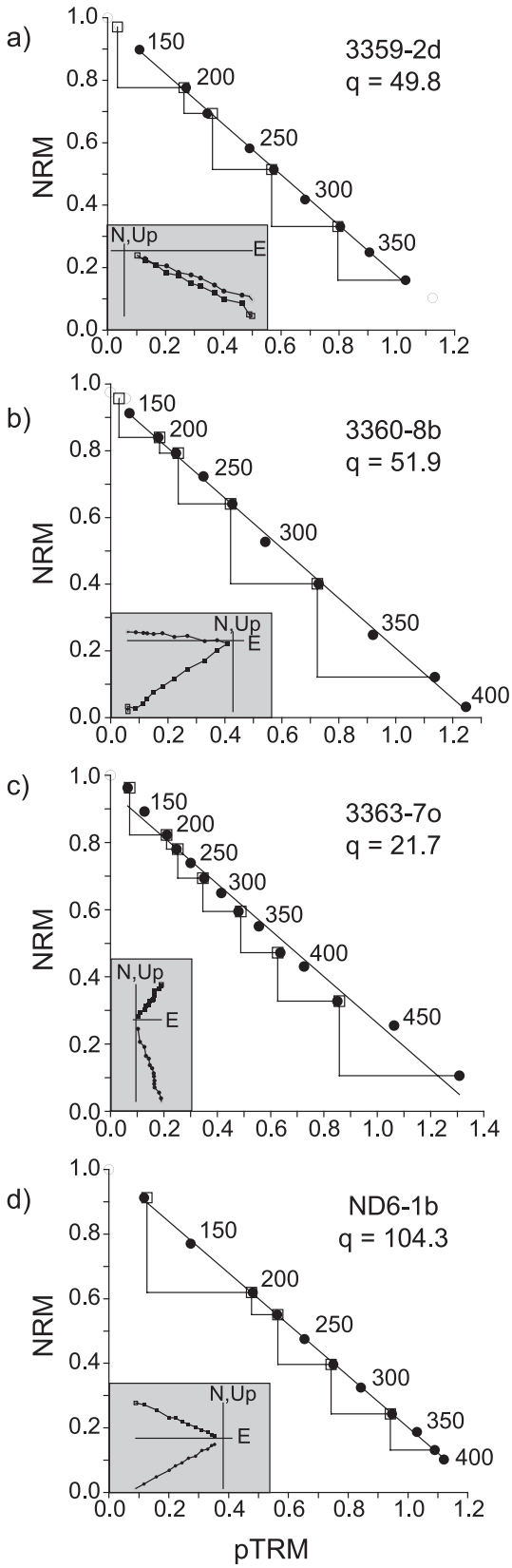

gether, these results strongly suggest the remanence carrier is SD, in complete agreement with previous results [e.g., *Pick and Tauxe*, 1993; *Zhou et al.*, 2000].

[18] Most specimens showed ideal behavior in the Thellier experiments. A single component magnetization unblocks over a range of temperatures from ~150–400°C for most samples, consistent with a magnetic mineralogy of low-titanium titanomagnetite or fine-grained magnetite. We note that the univectoral nature of the samples, combined with concordant paleointensities for all specimens from a given site, demonstrate that the samples were stationary while cooling through the blocking temperature range on the seafloor. At the very least, they were not part of a rapidly rotating lobe of lava, which would likely have acquired a complex, multicomponent remanence as, for example, may have been the case in a pillow fragment from the Juan de Fuca Ridge [*Kent and Gee*, 1996]. Most plots of NRM lost versus pTRM gained are highly linear, and most samples show no evidence of alteration during the experiment, as evidenced by the reproducibility between two in-field measurements at a given temperature (pTRM check).

[19] Given the generally high quality of the data, we applied fairly stringent reliability criteria: (1) The magnetization must be single-component. (2) The zero-field steps in the temperature interval selected for paleointensity interpretation must decay to the origin of a vector endpoint diagram (e.g., Figure 3, insets). This is taken as evidence that the magnetization represents an original remanence and is measured by the angle (α) between the principal component of the selected interval (anchored at the center of mass of the data) and the vector average of the data (anchored at the origin); we set a maximum value for α of ~5°. (3) To ensure sufficient reproducibility between two in-field measurements at a given temperature, the difference between repeat in-field steps normalized by the length of the selected NRM-pTRM segment must be less than 5%.

[20] Applying these selection criteria resulted in a reduction of our data set from 123 specimens to 86.

Figure 3. Representative NRM-pTRM plots. All values are normalized by the original NRM. Solid circles represent points used in calculation of best-fit slope. Squares are pTRM checks. Selected temperatures shown in °C. (inset) Vector endpoint diagrams showing demagnetization behavior of samples.

t2.1 **Table 2.** Paleointensity Results[a]

t2.2 Sample	d	F_{anc}	σ_b	F_{anc2}	σ_{b2}	loT	hiT	f	g	q	MAD	α	pTRM	F_m	σ	σ_e	$F_{m,b}$	$\sigma_{e,b}$
t2.3 3347-5a		38.6	0.32	38.4	0.85	100	375	0.86	0.88	90.6	1.2	0.8	0.5					
t2.4 3347-5c		39.0	0.44	38.3	1.53	100	375	0.69	0.86	50.8	1.8	2.3	1.9					
t2.5 3347-5e		36.1	0.52	36.3	0.90	100	375	0.81	0.88	51.8	1.2	1.3	2.0					
t2.6 3347-5f		38.0	0.92	37.1	2.82	100	375	0.68	0.86	23.5	1.7	1.5	2.1					
t2.7 3347-5g		37.2	0.76	38.1	3.02	100	450	0.85	0.89	36.2	2.0	2.7	2.4					
t2.8 3347-5h		35.5	1.00	35.5	3.15	100	375	0.88	0.87	27.6	2.8	1.4	3.3	37.9	1.2	0.5	37.3	1.0
t2.9 3348-5a		46.5	0.76	47.1	3.11	100	375	0.84	0.89	45.5	1.2	1.6	1.2					
t2.10 3348-5b		44.4	0.48	44.6	1.79	100	375	0.86	0.89	68.3	1.7	1.7	1.4					
t2.11 3348-5d		44.9	0.72	45.7	3.15	100	425	0.94	0.90	51.5	1.5	4.6	1.0					
t2.12 3348-5e		45.7	0.92	45.6	3.25	100	375	0.90	0.88	38.8	1.2	0.3	1.3					
t2.13 3348-5f		44.5	0.56	44.6	1.61	100	425	0.91	0.90	63.7	2.6	2.5	1.9					
t2.14 3348-5g		45.0	0.68	44.8	2.03	100	425	0.92	0.90	54.5	1.7	0.7	2.0					
t2.15 3348-5i		47.1	1.08	47.3	2.66	100	375	0.88	0.88	34.0	2.2	3.1	1.7	45.4	1.0	0.4	45.7	1.1
t2.16 3352-3a		39.9	0.52	41.2	4.21	100	475	0.93	0.88	63.9	2.7	1.4	1.2					
t2.17 3352-3b		38.7	0.24	38.9	1.58	100	475	0.92	0.90	130.9	2.4	1.4	1.2					
t2.18 3352-3c		39.9	0.32	40.2	1.64	100	500	0.93	0.88	101.2	2.1	2.3	1.2					
t2.19 3352-3d		38.1	1.16	37.3	3.20	100	500	0.96	0.89	27.7	2.3	2.1	1.7					
t2.20 3352-3e		36.2	1.00	35.4	1.11	100	500	0.93	0.87	29.6	3.7	3.7	3.3	38.6	1.5	0.7	38.6	1.4
t2.21 3353-7a		34.7	0.28	35.3	1.57	200	500	0.91	0.86	103.0	1.9	1.5	1.2					
t2.22 3353-7b		35.4	0.52	36.4	2.37	100	500	0.93	0.86	56.0	2.5	1.4	1.1					
t2.23 3353-7c		35.5	0.80	37.3	2.86	100	500	0.96	0.87	36.7	1.8	1.2	0.9					
t2.24 3353-7e		32.8	2.20	33.7	4.68	200	500	0.98	0.84	12.2	5.5	1.7	2.8					
t2.25 3353-7g		35.4	0.60	34.9	2.05	150	475	0.87	0.86	42.8	3.4	3.4	2.9					
t2.26 3353-7i		35.7	0.80	36.9	2.01	100	475	0.82	0.86	30.9	5.8	3.5	3.6	34.9	1.1	0.5	35.8	1.2
t2.27 3354-10d		56.1	0.88	55.6	1.68	100	375	0.61	0.85	33.6	1.1	1.2	2.3					
t2.28 3354-10g		63.7	1.48	65.3	2.83	100	450	0.79	0.90	30.0	1.8	1.5	1.8					
t2.29 3354-10h		54.7	1.00	55.6	2.85	100	375	0.87	0.88	41.3	1.6	5.1	1.1	58.2	4.8	2.8	58.9	3.1
t2.30 3356-1b		58.9	0.92	59.6	5.28	100	500	0.93	0.92	55.5	1.8	1.6	0.7					
t2.31 3356-1c		59.1	1.24	61.1	5.37	100	475	0.87	0.92	37.6	2.0	3.4	2.4					
t2.32 3356-1d		53.8	0.92	54.6	0.84	150	500	0.82	0.92	44.4	3.0	5.0	2.9					
t2.33 3356-1g		47.4	0.88	46.9	2.71	100	500	0.95	0.92	47.1	2.8	0.7	2.0					
t2.34 3356-1h		51.9	1.24	52.4	1.18	200	500	0.72	0.90	26.9	3.5	1.8	3.8	54.2	4.9	2.2	55.0	2.9
t2.35 3359-2a2	20	32.1	0.36	32.4	0.83	150	375	0.80	0.87	61.4	1.2	1.2	0.8					
t2.36 3359-2a3	20	32.3	0.44	32.8	1.21	150	400	0.91	0.88	56.4	2.4	1.3	1.2					
t2.37 3359-2b1	16	31.0	0.32	31.8	0.89	150	400	0.87	0.89	74.8	2.5	3.0	2.8					
t2.38 3359-2b2	16	31.7	0.36	32.0	0.83	150	400	0.83	0.88	63.0	3.7	2.1	0.8					
t2.39 3359-2b4	16	34.9	0.36	34.9	0.49	100	400	0.88	0.89	77.7	2.8	4.5	3.0					
t2.40 3359-2d	12	32.4	0.44	32.3	1.50	150	375	0.75	0.87	49.8	3.1	0.6	1.5					
t2.41 3359-2e1	12	32.1	0.60	32.5	0.77	150	400	0.86	0.89	40.3	2.3	2.0	2.0					
t2.42 3359-2h	8	29.6	0.52	29.3	0.81	150	375	0.75	0.87	36.1	4.3	1.2	4.7					
t2.43 3359-2j		33.7	0.40	33.8	0.86	100	350	0.81	0.87	58.2	1.4	0.8	0.6					
t2.44 3359-2k		34.2	0.52	34.5	0.93	150	375	0.83	0.87	46.7	2.1	1.1	0.5					
t2.45 3359-2m		31.2	0.60	31.2	1.21	200	400	0.74	0.87	32.4	2.0	0.9	2.2					
t2.46 3359-2n		31.9	0.40	32.0	1.01	100	400	0.94	0.89	64.8	1.5	0.6	0.9	32.3	1.4	0.4	32.5	0.5
t2.47 3360-8a		31.2	0.40	31.1	1.22	100	375	0.86	0.88	61.8	2.4	1.6	0.6					
t2.48 3360-8b		30.1	0.44	30.8	1.51	150	400	0.90	0.88	51.9	2.5	1.8	0.6					
t2.49 3360-8c		32.6	0.32	32.8	1.14	100	400	0.87	0.90	81.8	1.5	1.7	0.5					
t2.50 3360-8d		33.0	0.80	33.2	1.68	100	375	0.85	0.88	30.9	1.4	1.6	1.2					
t2.51 3360-8e		32.9	0.72	32.9	1.28	100	375	0.85	0.89	34.4	3.8	1.5	1.7	32.0	1.3	0.6	32.2	0.7
t2.52 3361-4(B)a	20	45.3	0.52	46.5	1.98	100	475	0.94	0.90	75.5	1.5	0.7	0.7					
t2.53 3361-4(B)b	16	39.7	1.16	41.4	5.36	100	475	0.95	0.90	29.5	2.4	2.1	2.0					
t2.54 3361-4a	20	44.6	1.12	44.9	2.77	100	450	0.86	0.90	30.5	3.0	2.3	2.8					
t2.55 3361-4b	16	45.7	0.48	45.6	2.12	150	450	0.73	0.89	63.6	4.0	0.9	2.3					
t2.56 3361-4c	16	33.6	0.72	34.6	2.70	150	475	0.91	0.89	38.8	2.9	4.3	2.7					
t2.57 3361-4e	12	40.4	2.12	39.4	2.72	100	475	0.82	0.90	13.9	7.4	3.6	4.0					
t2.58 3361-4r		49.2	0.92	50.3	2.68	150	425	0.87	0.89	41.5	1.7	0.7	1.1					
t2.59 3361-4s		48.9	0.88	51.2	4.64	150	450	0.88	0.89	43.4	2.0	1.4	1.1					
t2.60 3361-4t		45.5	0.64	45.3	2.65	150	450	0.83	0.89	51.9	4.1	2.0	1.9					
t2.61 3361-4u		48.2	0.64	49.6	2.55	150	475	0.94	0.90	65.2	1.7	1.5	1.1					
t2.62 3361-4v		44.3	0.84	44.4	3.73	100	475	0.89	0.89	42.4	3.6	1.5	1.5					
t2.63 3361-4w		47.5	1.04	47.9	5.10	100	475	0.94	0.91	38.4	2.1	1.4	1.6	44.4	4.5	1.2	45.1	1.7
t2.64 3363-7o		27.6	1.04	29.8	4.06	100	475	0.90	0.90	21.7	3.4	2.0	0.6					

Table 2. (continued)

Sample	d	F_{anc}	σ_b	F_{anc2}	σ_{b2}	loT	hiT	f	g	q	MAD	α	pTRM	F_m	σ	σ_e	$F_{m,b}$	$\sigma_{e,b}$
3363-7q		25.3	1.00	26.8	3.78	150	475	0.85	0.91	19.5	3.1	2.5	1.5					
3363-7r		27.7	0.96	29.1	3.08	150	475	0.89	0.91	23.7	2.9	2.7	1.3	26.9	1.4	0.8	28.6	2.2
ND18-1a		39.8	0.48	40.0	1.46	100	375	0.92	0.88	65.8	0.9	1.2	0.9					
ND18-1b		37.9	0.32	38.0	0.91	100	375	0.88	0.88	96.8	0.8	0.3	1.3					
ND18-1c		39.3	0.44	39.4	1.32	100	375	0.88	0.88	71.8	1.3	1.2	1.4					
ND18-1d		36.9	0.72	36.6	1.61	100	375	0.72	0.86	31.6	1.6	1.4	2.7					
ND18-1e		36.2	0.48	35.8	1.30	100	425	0.85	0.89	57.3	2.5	2.7	2.0					
ND18-1f		37.5	0.56	37.7	2.14	100	375	0.91	0.88	54.2	2.5	1.1	1.4					
ND18-1g		38.3	0.40	38.6	1.03	100	375	0.92	0.88	78.0	1.8	2.1	1.1					
ND18-1h		37.0	0.60	37.4	1.44	100	375	0.97	0.88	52.0	1.5	0.1	1.8	37.9	1.2	0.4	38.0	0.7
ND3-5c	8	28.6	0.60	29.0	1.39	100	375	0.85	0.88	35.4	3.5	2.9	3.6					
ND3-5d3	8	29.4	0.60	29.9	1.58	100	375	0.85	0.88	36.8	2.8	2.5	1.7					
ND3-5e	12	27.4	0.28	27.5	1.11	100	425	0.91	0.90	82.1	2.1	3.1	0.8					
ND3-5f	12	27.6	0.32	27.9	1.14	100	400	0.89	0.89	71.6	2.0	4.1	1.1					
ND3-5i	16	32.3	0.48	32.7	1.11	100	350	0.83	0.87	46.8	3.3	5.1	1.4					
ND3-5k		31.8	0.44	31.6	0.77	100	350	0.82	0.87	53.7	1.8	1.1	2.0					
ND3-5n		30.5	0.44	30.4	1.85	150	400	0.77	0.88	47.6	3.4	5.1	1.1					
ND3-5o		30.6	0.28	31.0	0.91	100	375	0.87	0.88	82.1	1.9	1.0	1.5	29.8	1.8	0.6	30.0	0.8
ND6-1a		32.9	0.36	33.1	0.98	100	400	0.76	0.87	57.9	1.1	0.7	1.0					
ND6-1b		31.9	0.20	31.7	0.56	100	400	0.81	0.88	104.3	1.7	1.5	0.8					
ND6-1d		34.1	0.68	34.2	1.35	100	375	0.87	0.89	39.7	1.7	1.7	1.3					
ND6-1e		35.5	0.52	35.3	1.58	100	425	0.91	0.90	54.6	1.7	0.5	2.1					
ND6-1f		36.8	0.56	37.1	1.63	100	425	0.90	0.90	53.0	1.6	0.7	2.3					
ND6-1g		32.4	0.32	31.9	1.60	100	475	0.89	0.90	79.4	1.0	1.4	0.9	33.9	1.9	0.8	33.9	1.0

[a] Notes: d, distance from inferred water-rock interface (mm); F_{anc}, paleointensity (μT); σ_b, standard error of the slope (μT) [*Coe et al.*, 1978]; F_{anc2}, σ_{b2}, paleointensity and standard deviation calculated as described in text; loT, hiT, lowest and highest temperature steps used in determining slope; f, g, q, NRM fraction, gap factor, quality factor [*Coe et al.*, 1978]; MAD, maximum angular deviation; α, angle between principle component and vector average (see text); pTRM, difference between repeat in-field steps (see text); F_m, site mean paleointensity; σ, standard deviation of mean; σ_e, standard error of mean; $F_{m,b}$, bootstrapped site mean (see text); $\sigma_{e,b}$, bootstrapped standard error.

Of these 86 remaining specimens, the minimum quality factor (q) as defined by *Coe et al.* [1978] is 12.2 and the average is 51.9. As a general rule, samples with the lowest q values also had the weakest NRM (moments $<6 \times 10^{-10}$ Am^2). All accepted paleointensity data and site means are given in Table 2, and a selection of demagnetization and NRM-pTRM plots are shown in Figure 3.

[21] Slopes on the NRM-pTRM plots were picked starting at 100–200°C after removal of a small viscous component, and ending at the highest step that still passed pTRM checks. This upper temperature limit was usually simply the highest temperature to which the sample was subjected. Values of f, the fraction of total NRM utilized in the Thellier analysis, average 0.86, indicating that the paleointensity results should be representative of field strength during cooling. Figure 4 shows histograms of both q and f, emphasizing the overall good quality of the results.

[22] While we applied objective criteria to sample and slope selection, we recognize that for some samples equally objective selection criteria can result in a significantly different slope. For example, one person might choose the data from 100°C to 475°C in sample 3363-7o (as shown in Figure 3c) because the last point at 475°C passes the pTRM check. This results in a paleointensity of 27.6 μT. Another person might include data only up to 425°C which maximizes q, resulting in a paleointensity of 31.6 μT. While the Coe parameter σ_b (Table 2) [*Coe et al.*, 1978], reflects the uncertainty in slope for a chosen set of points, there is usually a larger uncertainty associated with choosing one set of points as opposed to another set. We quantified this larger uncertainty by calculating slopes for all possible combinations of four or more points between 100°C and the highest temperature the sample was subjected to. If a selection of points fails the pTRM test, we threw it out. For all remaining slopes, we calculated a mean and standard deviation that we consider to be a better (and generally more conservative) estimate of the uncertainty in slope.

[23] To propagate these uncertainties into a site mean, we used these sample mean slopes and standard deviations as the starting point for a

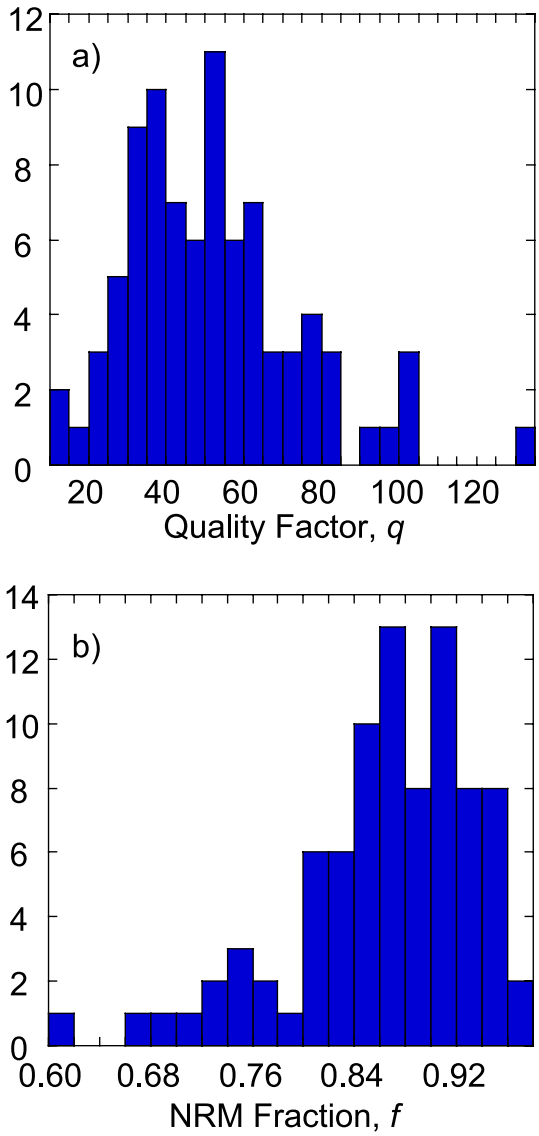

Figure 4. Histograms of the quality factor (q), and NRM fraction (f) of *Coe et al.* [1978] for all data passing the selection criteria (see text).

bootstrap analysis [*Efron*, 1982] of the site mean. Results of this exercise are shown in Table 2. In most cases, the bootstrapped site mean was nearly identical to the standard site mean, and the bootstrapped standard error was only slightly larger than the "regular" standard error. This implies that in most cases the slopes are relatively insensitive to our exact choice of points. In a few cases, however, the site mean is significantly different and/or had a standard error significantly larger than the non-bootstrapped case. We suggest that this larger error is a more accurate reflection of the true uncertainty of the mean.

[24] Site mean paleointensity results range from 28.6 to 58.9 μT. Comparison with global field models suggest that these values represent ages ranging from zero to >1000 years. Figure 5 shows the site mean paleointensity values (with 95% confidence intervals) plotted on a model curve of field intensity versus date based on the historical data of *Jackson et al.* [2000] from 1600 to 1990, and IGRF data from 1991 to 2005. We note that prior to 1840, this model is not constrained with direct intensity measurements, and instead combines direct observations of directional data with an assumption of a linear decay of the dipole term between 1600 and 1840. Furthermore, the model is constrained by few data in the Pacific prior to 1700. Therefore we have little confidence in the model values prior to 1840, although we have plotted the model back to 1600 for reference. We suggest only that it is likely the field was decreasing during this time interval, based on a compilation of regional archeomagnetic data [*Bowles et al.*, 2002]. The field intensity at 18°S in 1993 (when the first samples were taken during the NAUDUR cruise) was 31.3 μT (IGRF-9). Site means are plotted with 95% confidence bounds based on the bootstrapped standard error described above.

[25] One of the potential sources of uncertainty for this dating technique relates to cooling rate errors in the paleointensity estimate. If the glass consistently cools faster in nature than in our laboratory, the paleofield estimate (and, as a result, the age) will be biased too low. Furthermore, if a wide range of natural cooling rates results in significant within-site scatter, the use of this technique as an age discriminant becomes less powerful. For these reasons, it is necessary to understand what role (if any) cooling rate plays in paleointensity determinations in SBG. We will return to the discussion of paleointensity dating below.

4. Relaxation Geospeedometry

4.1. Theoretical Background

[26] As a silicate melt is quenched into a glass, it passes through a temperature region where it changes from equilibrium, liquid-like behavior to nonequilibrium glass-like behavior. The temperature at which this glass transition occurs is dependent upon the quench rate, and the frozen glass structure therefore reflects cooling history. We can take advantage of this structural "memory" to estimate the original cooling rate by reheating the

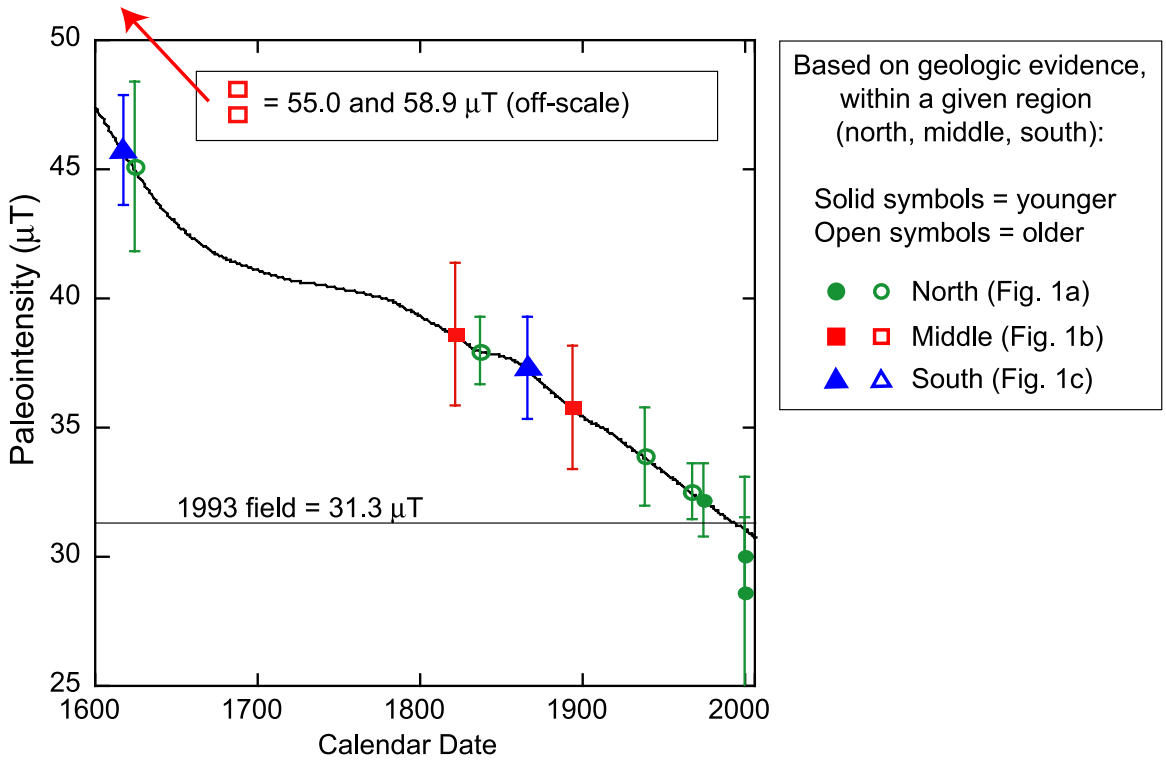

Figure 5. Site mean paleointensity values (error bars represent 95% confidence bounds) compared with gufm field model of *Jackson et al.* [2000] to 1990. IGRF data used from 1991 to 2005. Solid green circles denote samples from the Aldo Kihi flow field, thought to have erupted in the late 1980s to early 1990s. Note samples AL3354-10 (58.9 ± 6.2 μT, 2σ) and AL3356-1 (55.0 ± 5.8 μT, 2σ) not shown.

sample and monitoring some structure-dependent property (e.g., heat capacity) as the glass relaxes back into equilibrium [*Wilding et al.*, 1995].

[27] The structural evolution of a melt is often described using the concept of "fictive temperature" [*Tool*, 1946]. While the concept itself is an oversimplification, fictive temperature (T_f) can be thought of as the temperature at which a glass or melt would be in structural equilibrium. During cooling, T_f is thus always greater than or equal to the actual temperature, T. We let t represent time, and define the structural relaxation time, τ, as the time required for T_f to change by 1/e. If the cooling rate is approximated as a series of steps $\Delta T/\Delta t$, then at high temperatures and short relaxation times with respect to cooling rate ($\tau \ll \Delta t$), the melt is in equilibrium, and $T_f = T$ (Figure 6a). As the melt cools and τ approaches Δt, the melt is no longer in equilibrium, and T_f begins to depart from T ($T_f > T$). This corresponds to the onset of the glass transition. Finally, when $\tau \gg \Delta t$, the glass structure is frozen in and T_f has reached some limiting fictive temperature which remains constant with further decreasing temperature. The temperature at which the structure is frozen in depends on quench rate: the slower the rate, the longer the melt can stay in equilibrium, and the lower the limiting T_f (Figure 6c).

[28] On reheating, T_f follows a path reflective of the heating rate, as well as the previous cooling rate (Figure 6a). We exploit this "memory" effect on heating to provide an estimate of the quench rate. T_f can be indirectly monitored experimentally by measuring a structure-dependent property, such as enthalpy. In our case, we monitor changes in enthalpy by measuring heat capacity (the temperature derivative of enthalpy, $c_p = dH/dT \propto dT_f/dT$). As a glass sample is heated through the glass transition and the structure relaxes, c_p undergoes a step increase (Figure 6b). While the glass transition actually occurs over a range of temperatures, for practical purposes, we pick a single glass transition temperature, T_g, to be the peak of the endothermic hump. Because the exact geometry of the c_p heating curve depends on cooling history, we want to model the curve and solve for the best-fit prior cooling rate. For example, Figure 6d shows that for a constant

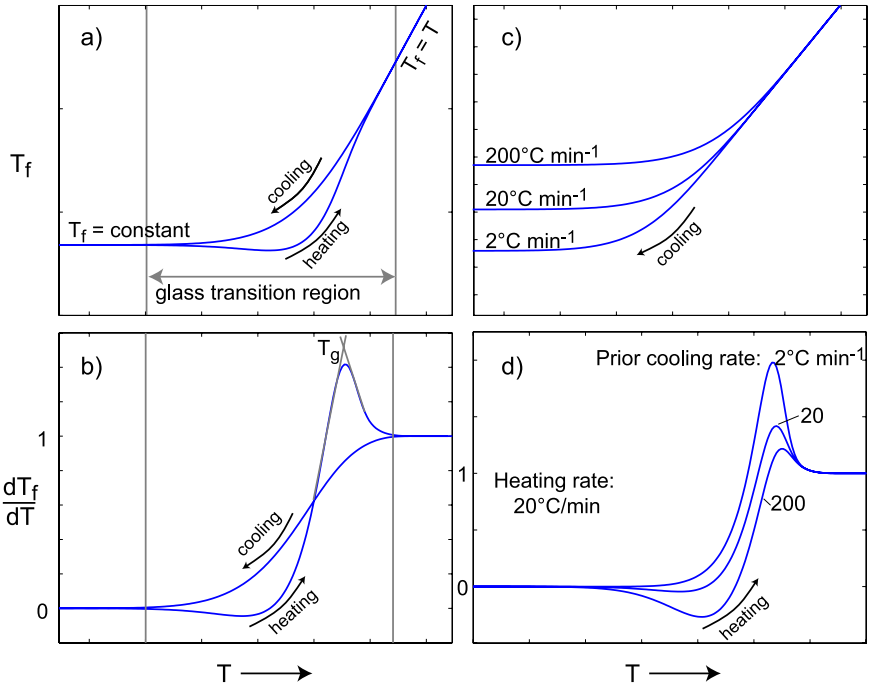

Figure 6. Evolution of fictive temperature (T_f) as a function of true temperature and heating/cooling rate (arbitrary temperature units). Note that in Figures 6a, 6b, and 6c the heating rate for each curve is equivalent to the previous cooling rate. (a) Fictive temperature versus true temperature on cooling and heating through the glass transition region. (b) The temperature derivative of T_f. This is indirectly monitored by measuring c_p (c_p = dH/dT). While the glass transition actually occurs over a range of temperatures, for practical purposes, we pick a single glass transition temperature, T_g, to be the peak of the endothermic hump. (c) Fictive temperature versus true temperature on cooling for 3 different quench rates. The faster the quench rate, the sooner T_f departs from the equilibrium condition of $T_f = T$, which results in a higher limiting fictive temperature. (d) dT_f/dT shows a similar rate-dependent progression on reheating, with faster rates resulting in higher values of T_g, as well as dramatically different peak heights. Note that the systematic change in peak height results from changing the prior cooling rate, but holding the heating rate constant.

heating rate, increasing the prior cooling rate results in a T_g peak of reduced amplitude, shifted to higher temperatures. The opposite is true for slower cooling rates.

[29] The mathematical treatment of this topic, including how we calculate and model c_p curves has been developed elsewhere [e.g., *DeBolt et al.*, 1976; *Wilding et al.*, 1995] and is summarized in Appendix A. We only note briefly here that calculation of the glass transition curve requires solving for four kinetic parameters that are dependent on sample composition. We find these parameters by cycling the sample through a series of controlled cooling and heating runs where the heating rate matches the previous (known) cooling rate. In this way we "calibrate" the relaxation response of the glass and can solve for the best-fit kinetic parameters. Once we have these parameters, we can solve for the original (unknown) cooling rate.

4.2. Technique

[30] After completion of the Thellier experiments, specimens were removed from their tubes and further subsampled for cooling rate analysis. Generally, two 25–60 mg subsamples from each successful Thellier specimen were subjected to the cooling rate experiment. In addition, several previously unheated specimens were also treated. No cooling rate analyses were performed on site AL33363-7 because so few successful paleointensity results were available.

[31] Heat capacity measurements for the cooling rate determinations were made on a Setaram DSC131 differential scanning calorimeter (DSC). Calorimetric calibration was performed with synthetic sapphire (NIST SRM720) and temperature calibration with the transition of standard materials. Glass chips were placed in stainless steel crucibles and heated at 10°C min^{-1} from 300 to 700°C in helium atmosphere. The samples were then cycled

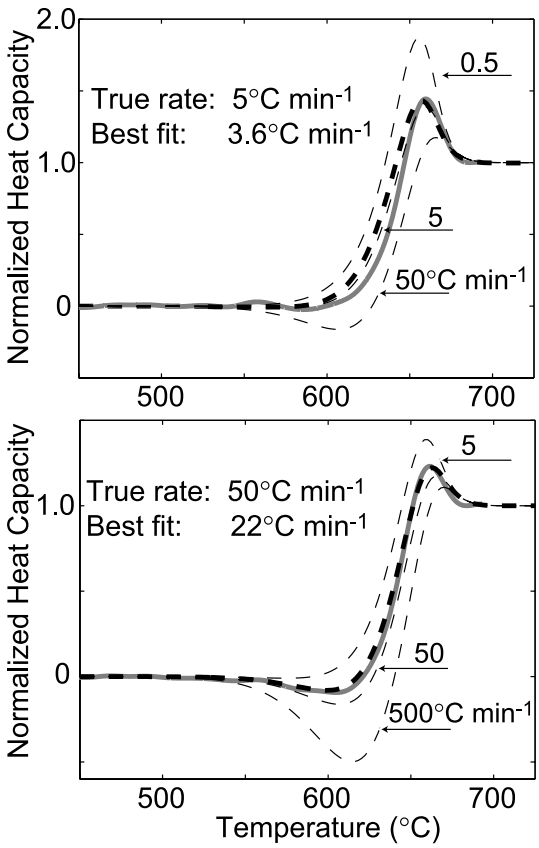

Figure 7. DSC data (in bold gray lines) plotted with best-fit model (bold, dashed black lines). (a) First heating (at 10°C min^{-1}) of sample that had previously been given a known cooling rate of 5°C min^{-1}. Thin, dashed black lines show modeled response one order of magnitude higher and lower than true rate. (b) Same as Figure 7a but for previous cooling rate of 50°C min^{-1}.

through a series of matched cooling and heating rates of 10, 15, 20, 25°C min^{-1} to calibrate the relaxation response of the sample and solve for the sample-specific kinetic parameters. Note that comparison of the measured c_p curves with the calculated model curves requires normalization of the measured curves to zero at temperatures below T_g and to one at temperatures above T_g.

[32] We have estimated error on the method in the following manner. A sample was cooled at a known rate (50°C min^{-1}, 30°C min^{-1}, or 5°C min^{-1}), and we then attempted to recover that rate with the method outlined above. Examples of two such attempts are shown in Figure 7. On the basis of this, we estimate the error in recovering the true cooling rate to be at least 0.3 log_{10} units, and note that the cooling rate at 50°C min^{-1} was consistently underestimated. This may be because the DSC cannot properly control cooling at such high rates, and the true cooling rate is <50°C. However, we cannot discount the possibility that the technique cannot properly estimate faster rates.

[33] A final concern is that the paleointensity experiments (which involve repeatedly heating the glass) might have altered the glass structure. Because most samples used in the cooling rate experiments were not heated above 400°C in the Thellier experiments (none were heated above 425°C), we did not expect the original glass transition interval in the samples (~550–650°C) to be significantly affected. To test this, we carried out a series of experiments on several previously unheated glass chips. The chips were cycled through a series of heatings, including one where they were held at 450°C for either 30 min or 2 hr before cooling. The results suggest that repeated heating to a temperature >100°C below the glass transition during the paleofield experiments likely had no significant affect on the original glass structure of the samples.

4.3. Cooling Rate Results

[34] Absolute cooling rates were determined for 55 out of 92 specimens. In the remaining cases, our model failed to adequately fit the data. Of the samples we were successful in modeling, cooling rates ranged from 10–330°C min^{-1}. Cooling rates along with best-fit kinetic parameters are given in Table 3.

[35] Because we were unable to make absolute cooling rate determinations on all specimens, we also examined a less highly processed parameter to evaluate relative cooling rates within a site. If we assume the glass from a given site has a homogenous composition, then variation in the temperature of the T_g peak should be related to cooling rate. Using the raw data, we take the difference (in degrees) between the position of the glass transition peak in the initial heating of the sample and the position of the peak in the controlled 10°C min^{-1} calibration curve. We choose the difference (rather than the absolute position of the T_g peak) to minimize possible slight effects related to drift in the temperature calibration of the DSC. The larger the temperature difference, the faster the original cooling rate was compared to 10°C min^{-1}. A negative difference implies a cooling rate slower than 10°C min^{-1}. This parameter (ΔT_g) is given in Table 3 for all samples.

[36] Figure 8 shows relative cooling rate (ΔT_g) plotted against absolute cooling rate for all speci-

Table 3. Cooling Rate Results[a]

	Dist., mm	ΔT_g	°C min^{-1}	x	β	$-\log_{10}$ A	ΔH*, kJ
3359-2a1(1)	20	3.4	73	0.65	0.65	37.6	691.4
3359-2a2(1)	20	2.1					
3359-2a2(2)	20	1.5					
3359-2a3(1)	20	3					
3359-2b1(1)	16	2.2	27	0.93	0.70	28.3	527.6
3359-2b1(2)	16	2.6	59	0.80	0.70	28.9	537.5
3359-2b2(1)	16	3.2	85	0.80	0.74	29.4	546.0
3359-2b2(2)	16	3.6	85	0.93	0.74	28.1	523.3
3359-2b4(1)	16	2.1	24	0.57	0.67	33.9	625.2
3359-2c(1)	12	2.6					
3359-2c(2)	12	2.0					
3359-2d(1)	12	2.9	228	0.50	0.74	31.5	583.5
3359-2d(2)	12	3.0	83	0.69	0.76	28.0	523.2
3359-2e1(1)	12	2.0	71	0.74	0.73	28.2	525.0
3359-2e1(2)	12	3.2	137	0.58	0.79	25.1	471.5
3359-2e2(1)	12	3.4	89	0.70	0.63	36.4	670.3
3359-2h(1)	8	3.7	78	0.90	0.70	34.3	634.4
3359-2h(2)	8	3.6					
3359-2i(1)	4	4.5	107	0.86	0.64	33.7	623.5
3359-2i(2)	4	3.5	36	0.90	0.58	35.5	653.5
3359-2k(1)		1.8	31	0.77	0.69	32.9	607.7
3359-2k(2)		1.7					
3359-2l(1)		3.1	71	0.72	0.78	25.7	482.1
3359-2l(2)		3.9	80	0.72	0.74	28.9	537.5
3359-2m(2)		3.8	65	0.62	0.70	31.9	591.1
3359-2n(1)		4.4					
3359-2n(2)		3.6					
3360-8a(1)		0.7	26	0.77	0.70	31.5	584.8
3360-8a(2)		2.5	70	0.78	0.63	28.7	533.8
3360-8b(1)		1.3	54	0.72	0.58	30.7	568.6
3360-8c(1)		−0.5	22	0.76	0.76	30.3	562.5
3360-8c(2)		2.1	16	0.86	0.68	29.0	539.5
3360-8d(1)		0.6	24	0.75	0.81	25.8	484.1
3360-8d(3)		1.1	10	0.61	0.64	34.5	635.7
3360-8e(1)		2.5	25	0.98	0.71	28.2	524.8
3361-4a(1)	20	4.2					
3361-4b(1)	16	3.1	34	0.71	0.64	32.7	597.3
3361-4b(2)	16	2.8	38	0.98	0.67	29.8	546.8
3361-4c(1)	16	2.4	72	0.86	0.68	29.8	546.6
3361-4c(2)	16	2.2	41	0.81	0.64	33.6	612.1
3361-4e(1)	12	4.0	65	0.73	0.71	29.6	542.9
3361-4e(2)	12	1.9					
3361-4r(1)		1.5	40	0.63	0.76	26.7	492.9
3361-4r(2)		1.3	38	0.81	0.69	27.7	510.8
3361-4s(1)		2.1					
3361-4s(2)		2.4					
3361-4t(1)		2.1	29	0.63	0.70	30.7	564.2
3361-4t(2)		2.4	39	0.65	0.69	32.0	585.3
3361-4u(1)		2.4					
3361-4u(2)		1.2	118	0.75	0.73	29.7	544.7
3361-4(B)a(1)	20	2.7	64	0.76	0.67	31.1	569.4
3361-4(B)a(2)	20	1.9	67	0.57	0.64	27.9	512.0
3361-4(B)a(3)	20	1.4					
3361-4(B)a(4)	20	1.6					
3361-4(B)b(1)	16	2.9					
3361-4(B)b(2)	16	3.6					
3361-4(B)d(1)	16	3.1					
3361-4(B)d(2)	16	4.3					
3361-4(B)l(1)	4	4.1					
3361-4(B)l(2)	4	7.0					
ND3-5b(1)		4.7	65	0.65	0.65	36.1	663.5
ND3-5b(2)		2.6	327	0.57	0.67	32.7	602.5

Table 3. (continued)

Dist., mm	ΔT_g	°C min^{-1}	x	β	$-\log_{10}$ A	ΔH*, kJ
ND3-5b(3)	1.4	40	0.82	0.77	26.0	485.6
ND3-5c(1)	4.3					
ND3-5c(2)	1.7	39	0.81	0.65	32.3	596.3
ND3-5c(3)	4.7	54	0.84	0.70	30.4	561.6
ND3-5d1(1)	2.9	54	0.73	0.66	34.2	630.3
ND3-5d2(1)	3.7					
ND3-5d3(2)	−0.4	34	0.88	0.67	28.7	532.3
ND3-5e(1)	2.8	76	0.87	0.66	31.8	587.0
ND3-5e(2)	2.6	40	0.93	0.72	27.5	511.9
ND3-5f(1)	3.5	144	0.57	0.67	28.4	527.0
ND3-5f(2)	2.2					
ND3-5g(1)	4.1	56	0.76	0.61	39.1	715.9
ND3-5i(2)	3.1	201	0.85	0.60	34.8	637.6
ND3-5j(1)	3.1					
ND3-5J(2)	3.6					
ND3-5k(1)	4.0	104	0.70	0.76	26.9	501.6
ND3-5k(2)	4.4					
ND3-5l(1)	2.9	83	0.66	0.75	28.4	528.3
ND3-5n(1)	3.9	142	0.84	0.74	27.1	505.9
ND3-5n(2)	3.6	85	0.99	0.68	26.9	501.0
ND3-5o(1)	2.3					
ND3-5o(2)	2.3					
ND6-1a(1)	0.0	19	0.84	0.73	26.2	487.4
ND6-1a(2)	−0.5					
ND6-1b(1)	0.2					
ND6-1b(2)	1.0					
ND6-1d(1)	2.1					
ND6-1d(2)	3.7					
ND6-1e(1)	3.1					
ND6-1f(1)	1.6	45	0.83	0.75	27.7	515.3
ND6-1f(2)	0.2					

[a] Dist., mm, distance from inferred water-rock interface; ΔT_g, relative cooling rate (see text); °C min^{-1}, modeled cooling rate; x, β, A, ΔH*, best-fit kinetic parameters (see text).

mens where both are available. Scatter in the correlation is not unexpected, because different sample chemistry will result in a different relationship between the two estimates. We also calculate and plot curves encompassing the range of expected values based on the range of kinetic parameters found in modeling the absolute cooling rates (see Appendix A, Table 3). Most data fall within these bounds, with a few exceptions. We excluded from further analysis data that fall outside these bounds. While the scatter suggests that ΔT_g may not be an ideal parameter for examining cooling rate variations, it is much more straightforward to calculate than absolute cooling rate, and should allow us to distinguish trends within a given sample.

5. Discussion

5.1. Absolute Cooling Rates

[37] The range of absolute cooling rates we find (10–330°C min^{-1}) spans ~1.5 orders of magnitude. Furthermore, while the absolute cooling rate determinations were not possible for many specimens, we can safely say that nearly all rates were faster than 10°C min^{-1} (the slowest calibration cooling rate). This is inferred from the fact that $\Delta T_g > 0$ in almost all cases. These rates are faster than those found by *Wilding et al.* [2000] in hyaloclastites, most of which fall between 1.5–7°C min^{-1}, with one sample at 25°C min^{-1}.

[38] Although the absolute cooling rates for our glass samples exceed those of *Wilding et al.* [2000], simple thermal models indicate such high rates are not unexpected. Following *Turcotte and Schubert* [2002], we calculate instantaneous cooling of a half-space, assuming an eruption temperature of 1150°C, and ignoring heat of fusion. We repeat the calculations for two values of thermal diffusivity ($\kappa = 5 \times 10^{-7}$ and 8×10^{-7} m^2 s^{-1}), approximately spanning the range found in the literature for basalt [e.g., *Turcotte and Schubert*, 2002; *Kinoshita et al.*, 1996; *Vosteen and Schellschmidt*, 2003]. Figure 9a shows the results of these calculations plotted as cooling rate versus

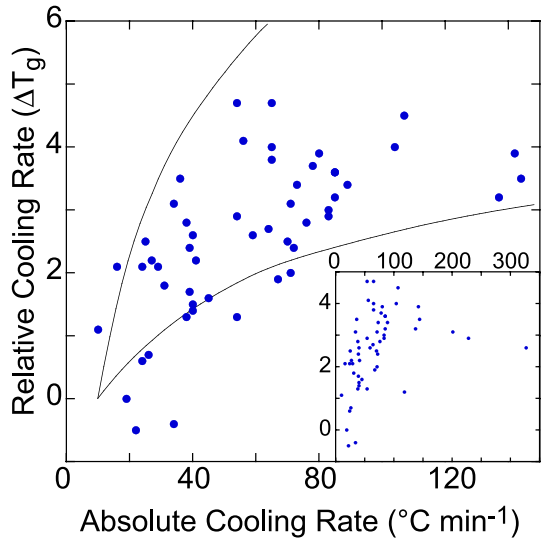

Figure 8. Absolute cooling rate (as determined by finding best-fit model c_p curve) versus relative cooling rate, as measured by ΔTg (see text). Blue dots show all data where both types of estimate are available. Solid curves show calculated range of the relationship (for rates >10°C min^{-1}), given the range of kinetic parameters found (see Table 3, Appendix A).

temperature for three depths below the water-rock interface. At the glass transition temperature (650°C), cooling rates may be as high as 400–700°C min^{-1} at 0.5 cm below the interface.

[39] In Figure 9b, we plot the cooling rate at 650°C versus depth below the water-rock interface, highlighting the range of absolute cooling rates found in our glass samples. This plot suggests that the range of rates we measure is consistent with cooling at ~0.5–4 cm below the interface. Similar calculations for a sphere [*Yovanovich*, 1996] of radius 0.25 m, to approximate a pillow geometry, are also shown.

[40] The above calculations are inconsistent with the fact that glassy margins more than a ~2 cm thick are rarely observed in mid-ocean ridge basalts. However, as mentioned above, our calculations ignore the heat of fusion and assume all heat is instantaneously removed from the water-rock interface. Any departure from this ideal case will lead to slower cooling at all depths, which will shift the curves in Figure 9b down. Furthermore, some of our experimental determinations of cooling rate may be underestimated, based on the results of our error analysis (above). Taking these two factors into consideration, the range of cooling rates we find is entirely compatible with what might be expected in a flow quenched at the seafloor.

5.2. Relative Cooling Rates

[41] While absolute cooling rate estimates were made for only about half the specimens, we have many more relative cooling rate estimates. We can test whether or not our relative cooling rate parameter (ΔT_g) is capturing cooling rate variations by looking first at the oriented transects. In these cases we predict cooling rates to be faster closer to the inferred water-rock interface. Figure 11 shows relative cooling rate plotted against distance from the interface for each sample for which data are available. Two of the three oriented samples (AL3359-2 and AL3361-4(B)), show a trend consistent with our expectations. Though scattered, a negative correlation is found between cooling rate and distance. This correlation is significant at the 99% confidence level for site AL3359-2 and for the transect B from AL3361-4. While the few data from the transect A from AL3361-4 do not show a statistically significant correlation, when combined with the results from transect B, the correlation is significant at the 99% confidence level. We note that while the true underlying correlation between ΔT_g and distance is not linear, given the scatter in the data, this is a close enough approximation for our purposes.

5.3. Cooling Rate Effects on Paleointensity

[42] One of the things we want to determine is whether the rapid natural cooling of the glass will lead to a bias in the paleointensity data. To determine this, we need to know (1) how the cooling rates found at the glass transition (~650°C) translate to cooling rates over the dominant magnetic blocking temperature range (~200–400°C) and (2) what the cooling rates are in our laboratory ovens over the same temperature interval. To estimate the former, we extrapolate cooling rates found at 650°C to 400°C with calculations as described above (Figure 9a, inset). Instantaneous cooling of a half-space suggests that rates at 400°C would be about half those found at 650°C. This means that our absolute cooling rates of 10–330°C min^{-1} at 650°C equates to ~5–170°C min^{-1} at 400°C.

[43] To better determine laboratory cooling rates, we directly measured temperature in the Scripps oven during forced air cooling, with a thermocouple packed into a glass tube in a manner similar to the glass samples. Results show a significant cooling rate gradient from one end of the oven to the

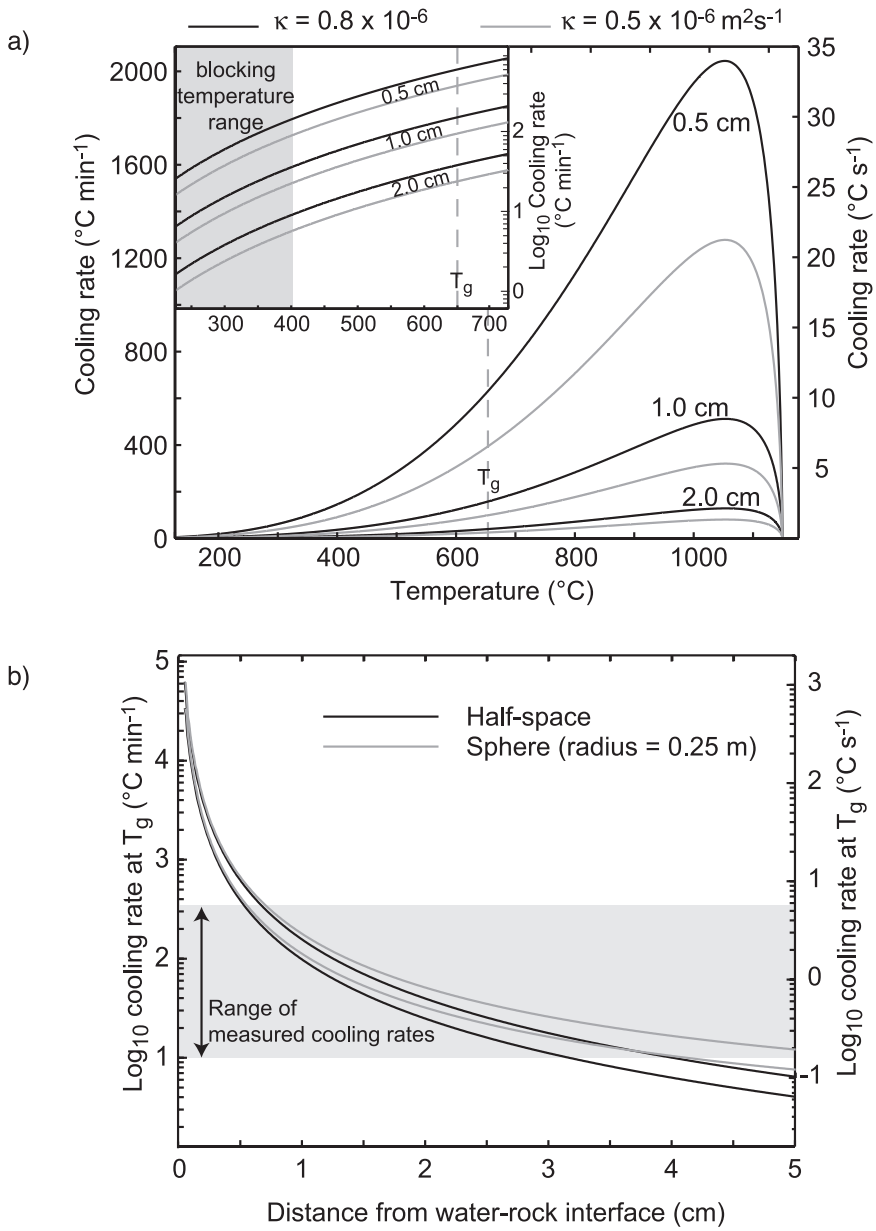

Figure 9. (a) Calculated cooling rate versus temperature for an instantaneous cooling of a half-space with magma emplaced at 1150°C (see text). Three sets of curves are shown for cooling profiles at 0.5, 1.0, and 2.0 cm from the water-rock interface. Black curves are calculated with $\kappa = 0.8 \times 10^{-6}$ m^2 s^{-1}; gray lines are calculated with $\kappa = 0.5 \times 10^{-6}$ m^2 s^{-1}. Inset shows $\log_{10}$ cooling rate for the temperature region of interest. (b) Calculated cooling rate versus distance inward from water-rock interface. Black lines are calculated from instantaneous cooling of a half-space. Gray lines are calculated from instantaneous cooling of a sphere with radius of 0.25 m. Cooling profiles bracket range of rates found using $\kappa = 0.5–0.8 \times 10^{-6}$ m^2 s^{-1}. Shaded area represents range of measured cooling rates.

other (Figure 10). Cooling rates at 400°C are 185°C min^{-1} closest to the fan and 65°C min^{-1} ~24 cm farther away from the fan. At 200°C, rates are ~50 and 30°C min^{-1}, respectively. These rates are approximately equal to or slightly faster than the ancient rates found in the cooling rate experiments, suggesting that we are likely not underestimating paleointensity, and may be slightly overestimating it. This takes into account only the cooling rates we were successful in modeling. Because our error analysis of the modeling procedure suggests that the faster rates are more difficult to estimate, there may well be some natural cooling rates faster than our laboratory rates. Nevertheless,

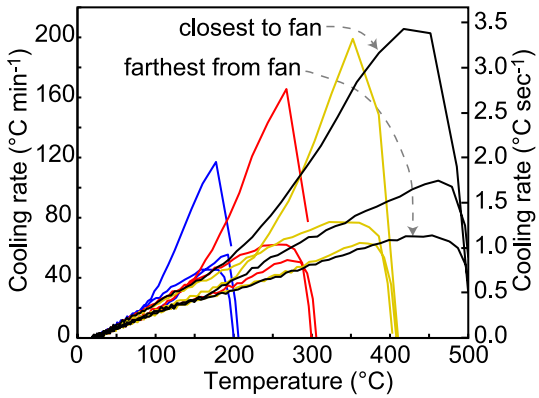

Figure 10. Cooling rates inside oven. Cooling rates were measured at three positions corresponding to sample locations closest and farthest from the fan, as well as an intermediary position. This was repeated starting cooling from 500°C (black), 400°C (gold), 300°C (red), and 200°C (blue). With the exception of the position closest to the fan, cooling rate shows little dependence on this initial temperature.

the data suggest that there is unlikely to be a systematic low bias to the paleointensity data.

[44] In addition to a bias in the paleointensity estimate, variation in cooling rate may lead to within site scatter in paleointensity estimates. If paleointensity is to be used as a dating tool, we would like the data to be as accurate and precise as possible. If natural cooling rates in our samples vary by 1.5 orders of magnitude, we should be able to test whether or not this range of cooling rates is reflected in paleointensity variation. According to theory, we could possibly explain up to ~10% of the scatter in the paleointensity data with cooling rate variation.

[45] We return to the oriented transects (Figure 11), where we can again make a clear prediction: paleointensity estimates should increase with decreasing cooling rate and thus with distance from the water-rock interface. As above with cooling rate versus distance, we do not expect the correlation to be linear. However, the most strongly nonlinear portion should be closest to the margin where we have few to no paleointensity data. Site AL3359-2 has a (weak) positive correlation between paleointensity and distance. This correlation is significant only at the 80% confidence level, but the magnitude of the effect is approximately what we would expect (~5–10%). The fact that there are so few paleointensity data available for site AL3361-4 is reflected in the even lower confidence level (75%) for the correlation. However, at both sites, a negative correlation between cooling rate and distance is matched by a positive correlation between paleointensity and distance.

[46] The rest of our specimens have no orientation information, but if cooling rate has a significant effect on paleointensity scatter, there should be a negative correlation between paleointensity and cooling rate. Figure 12 plots all paleointensity data

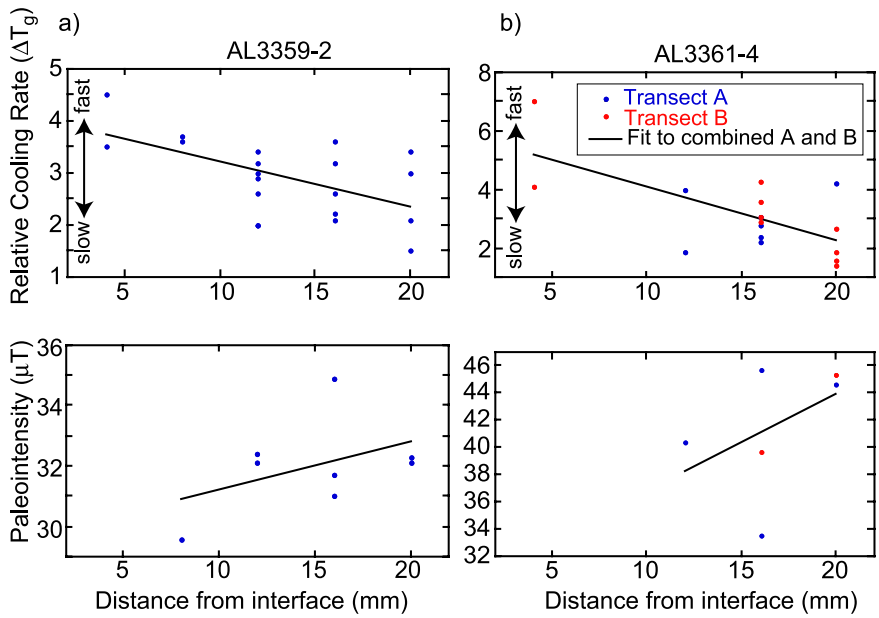

Figure 11. Relative cooling rate (as measured by ΔT_g; see text) and paleointensity versus distance from inferred water-rock interface on transects taken from samples (a) 3359-2 and (b) 3361-4 (two transects: A and B).

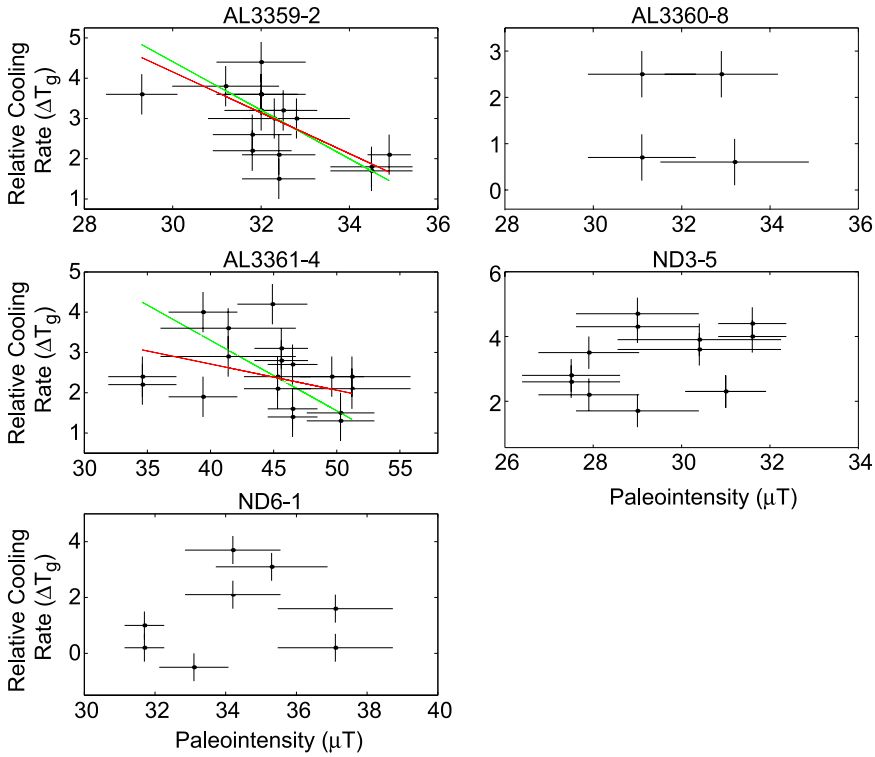

Figure 12. Paleointensity versus relative cooling rate (as measured by ΔT_g; see text). Larger ΔT_g is faster cooling rate. Best-fit correlations shown for sites AL3359-2 and AL3361-4; red line weights all data equally, green line weights data according to their relative errors in both x and y (R. L. Parker, personal communication, 2004). Errors in paleointensity are $1\sigma_{b2}$ (see Table 2), calculated from bootstrapped slope estimate of NRM versus pTRM plots (see text and Table 2). Errors in ΔT_g are estimated as a constant 0.5 units.

against relative cooling rate for each site. As above, sites AL3359-2 and AL3361-4 show a statistically significant correlation at the 99% and 80% confidence levels, respectively. The correlation is in the direction that we expect: increasing paleointensity with decreasing cooling rate. We found a similar correlation between absolute cooling rate and paleointensity, though at a lower significance level.

[47] The remaining sites, however, show no correlation between paleointensity and cooling rate. The large degree of scatter in the data is perhaps not unexpected. Specimens used for paleointensity analysis are up to ~1 g and 1–2 cm in length, while specimens for cooling rate analysis are generally <50 mg. As calculated above, cooling rates spanning >1.5 orders of magnitude can be found in a 2–3 cm interval in the cooling magma. Thus significant variations in cooling rate on a millimeter scale may be averaged out in the larger samples used for paleointensity analysis. In the transects from sites 3359-2 and 3361-4, we purposely sampled the glass parallel to an estimated cooling front, which should serve to minimize cooling rate variation within individual specimens. In the remaining cases, however, sampling was completely arbitrary with respect to the cooling front, leading to a wider range of cooling rates within a single paleointensity specimen. It may be that with such a low signal-to-noise ratio, the relatively few data from sites ND3-5, ND6-1, and AL3360-8 are insufficient to capture the underlying relationship. Some of the scatter may also be explained by variations in the laboratory cooling rate during the paleointensity experiments. A cooling gradient within the oven will result in within site scatter if specimens are distributed throughout the oven.

[48] While correlations between ancient cooling rate and paleointensity may be weak, we suggest that in at least some cases, cooling rate can have an identifiable effect on paleointensity in SBG. This is bolstered by the fact that in spite of the given factors that can lead to significant scatter in this correlation, we still see a consistency between cooling rate, paleointensity, and distance from margin in the cases where we know what the

relative correlations should be. However, in most cases, sampling techniques for paleointensity will tend to average out the effect.

5.4. Paleomagnetic Dating

[49] The above analysis of cooling rates, both in the laboratory and in nature, suggest that in extreme cases, a cooling rate effect could lead to significant scatter in the data, perhaps up to 15%. However, because the natural cooling rates appear to span the range of laboratory cooling rates, we suggest that there is not likely to be a significant bias (high or low) in a site mean, given a sufficient number of specimens per site. Moreover, glasses quenched at the fastest rates invariably have lower magnetizations, often making them unsuitable for paleointensity analysis. Therefore the effective range of cooling rates in SBG samples used for paleointensity studies is likely to be smaller than the full range of cooling rates found throughout the glassy margin.

[50] Having eliminated cooling rate as a potential source of bias, we return to our discussion of paleomagnetic dating. Presently, radiometric dating [*Rubin et al.*, 2001; *Bergmanis et al.*, 2004] can only provide a very rough idea of age (younger or older than 100 years) for these young flows. As demonstrated in Figure 5, not only can we make relative age assignments, but we can also estimate an eruptive date by comparing site paleointensities to global paleomagnetic models.

[51] On the basis of this analysis, samples AL3360-8, AL3363-7, and ND3-5 (shown as solid green circles in Figure 5) overlap the 1993 value at the 95% confidence level, and are consistent with eruptive dates ranging from 1944 to present. These three samples were taken from the Aldo-Kihi flow field (thought to have been erupted in the late 1980s or early 1990s). The remaining samples can be statistically distinguished from the present-day value, and have 95% confidence bounds ranging from ~40–220 years. Sites AL3361-4 and AL3348-5 have means consistent with eruptive dates of ~1625 and ~1620, but as the model is poorly constrained prior to 1840, the true age uncertainty is significantly greater than that suggested by standard error. However, if we assume (on the basis of available archeointensity data, such as that summarized by *Bowles et al.* [2002]) that the field intensity has been decreasing for the past ~500–1000 years, we can at least say that these two sites are significantly older than sites with lower paleointensity values. Finally, samples AL3356-1 and AL3354-10 (taken from the older, more tectonized region) have paleointensity values significantly higher than any represented by the field model. Again, on the basis of the archeointensity data, we suggest that these samples are associated with the high in paleointensity ~500–2000 ybp.

[52] These paleointensity ages agree well with the geological observations. The three samples taken from the presumed youngest Aldo-Kihi flow field have the lowest paleointensities with corresponding ages that overlap the estimated eruption date(s). The three samples taken to the north and south of the Aldo-Kihi flow (ND6-1, ND18-1, and AL3359-2) have higher mean values, consistent with eruption dates of ~1930, ~1840, and ~1965, respectively. AL3361-4, taken west of the axis, has a paleointensity indicating that it is several hundred years older than samples taken from the young, on-axis flows. In no case does the ordering of ages based on paleointensity disagree with the stratigraphic ordering of the sites based on the geologic observations. The only notable exceptions are samples AL3347-5 and AL3348-5, taken from the South Hump area (Figure 1c) and represented by blue triangles in Figure 5. These two sites have significantly different paleointensities, suggesting that even though there is no geological evidence for a boundary between these two sites, the northern area was erupted up to several hundred years prior to the southern area. This is consistent with the geochemical differences between the north and south areas, as well as the vertical offset in the AMC reflector.

[53] The paleointensity data are also consistent with available radiometric ages determined by $^{210}Pb/^{226}Ra$ disequilibria [*Rubin et al.*, 2001; *Bergmanis et al.*, 2004]. Sites AL3363-7 and ND3-5 (with paleomagnetic "dates" indistinguishable from the 1993 value), and ND6-1 (paleomagnetic date: ~1930) have ^{210}Pb deficits consistent with ages of <100 years. Sites ND18-1 (~1840) and AL3361-4 (several hundred years old) show no disequilibria, consistent with ages >100 years. However, because of ambiguities in the processes that result in the disequilibria, the lack of disequilibrium does not preclude the possibility that the samples are actually younger than 100 years old.

[54] It should be noted that while the three samples taken from the single Aldo Kihi flow field all overlap the expected eruption date at the 95% confidence level, the mean paleointensities differ

by ~10%. Two of these (AL3360-8 and ND3-5) have statistically distinct means (at the 95% confidence level, based on a *t* test). While observations suggest that the flows composing the Aldo Kihi flow field are distinctly younger than the surrounding flows, there is little to indicate the actual duration of the eruption period. It may have been only 5–10 years, but it may have been sufficiently long to result in statistically distinct site means. However, we must also consider factors that could cause the glass to record something other than the main field at the time it was quenched. Although we stated above that we do not expect cooling rate effects to result in a significant bias between a single site and the true field value, even a small (<5%) bias could resolve the discrepancy between the two site means in this case.

[55] Another possible explanation is a local field effect. The flows were emplaced on a magnetic terrain, which will cause some deflection of the ambient magnetic field. If the flows are smooth and flat, this effect should be minimal. However, pillows, lobes, lava pillars or walls will cause a terrain effect. The magnitude of the effect depends on how magnetic and rugged the terrain is and how thick the newly emplaced flow is. The upper quenched surface of a flow that is meters thick may be buffered from the strongest terrain effect, while thin sheet flows a few centimeters thick will be more strongly affected. *Sinton et al.* [2002] find evidence that the Aldo Kihi flows are locally >12 m thick. Near-bottom (5–40 m elevation) direct field measurements at 17°28.5′S (which includes part of the Aldo Kihi flow field) show that the terrain effect may be up to ~1 μT at these elevations [*Shah et al.*, 2003]. We therefore believe the effect here to be less than the 2σ standard error of the mean for most sites, but the exact magnitude of the effect bears further study.

[56] Finally, one criticism of paleointensity estimates from SBG has been the suggestion that the remanence is a grain-growth chemical remanence (CRM) formed at low temperatures, rather than a primary TRM [*Heller et al.*, 2002]. This is an important point, because glass samples with a CRM would give paleofield estimates significantly lower than the expected value [*Stacey and Banerjee*, 1974].

[57] *Heller et al.* [2002] speculate that the low-Ti titanomagnetite in SBG must form at low temperatures because it is not an equilibrium phase in the melt [*Buddington and Lindsley*, 1964]. However, because glass is not an equilibrium phase, one should not expect the phase equilibria of *Buddington and Lindsley* [1964] to apply. Other strong evidence in favor of a primary TRM is summarized by *Tauxe and Staudigel* [2004]. We only draw attention here to the transmission and analytical electron microscopy work of *Zhou et al.* [2000]. They have shown that both grain size and average Ti-content decrease (while scatter in Ti content increases) as the margin of a basalt pillow is approached from the interior. None of the grains show evidence for low-temperature oxidation. *Zhou et al.* [2000] convincingly explain these observations as resulting from an increase in cooling rate as the rim is approached. They call on reasonable thermodynamic and kinetic controls that together result in lower Ti content with increased cooling rate.

[58] Data from the oriented glass transects in this paper provide further evidence that the remanence in SBG is a primary TRM. All of our transects display increasing NRM and magnetic grain size with depth within the glassy margin. These trends are the opposite of what might be expected if the remanence were a grain-growth CRM resulting from some kind of weathering or bio-mediated process, as suggested by *Heller et al.* [2002]. In that case, magnetization should be strongest in the glass closest to the margin where the glass interacts with water. Furthermore, paleointensity determinations from the recent Aldo Kihi flow are completely consistent with the presumed date(s) of eruption. A CRM would more likely have resulted in values significantly and consistently lower than present-day values. As this is not observed, we conclude that remanence is a primary TRM.

6. Conclusions

[59] In conclusion, we find a range of absolute cooling rates (10–330°C min^{-1}) at the glass transition consistent with the values predicted from calculations of cooling within the glassy margin of a flow emplaced on the seafloor. These rates are also approximately equal to (or slightly lower than) the measured laboratory rates, but faster rates are also likely, though not resolvable with our technique.

[60] In the sites we systematically sampled parallel to the inferred water-rock interface, we find a negative correlation between relative cooling rate and distance from the interface matched by a positive correlation between paleointensity and distance. The corresponding correlation between

Table 4. Symbols Used in This Paper

	Definition	Units
A	"preexponential" factor	s^{-1}
c_p	heat capacity	J K^{-1}
H	enthalpy	J
ΔH^*	activation enthalpy	J mol^{-1}
q	heat and/or quench rate	K s^{-1}
R	gas constant	J mol^{-1} K^{-1}
t	time	s
T	temperature	K
T_g	glass transition temperature	K
T_f	fictive temperature	K
x	factor partitioning the temperature versus structural dependence of τ_o ($0 \leq x \leq 1$)	
β	factor related to width of relaxation spectrum ($0 < \beta \leq 1$)	
κ	thermal diffusivity	m^2 s^{-1}
ϕ	equilibrium relaxation function	
τ	relaxation time	s
τ_o	"characteristic" relaxation time for enthalpy	s

cooling rate and paleointensity, while weak, has a magnitude approximately equal to the cooling rate effect predicted by theory (i.e., ~5–10% change in paleointensity for a cooling rate change of 1.5 orders of magnitude).

[61] A number of factors can lead to scatter in this correlation, however, including variation in laboratory cooling rates, and the small scale of natural cooling rate variation in comparison to the size of the paleointensity samples. As a result, most cooling rate effects are likely to get averaged out given a sufficient number of specimens per site, and a systematic low bias to paleointensity results is unlikely.

[62] The results of the cooling rate analysis suggest that the magnitude of any cooling rate effect (in either bias or scatter) is unlikely to negatively impact our ability to use paleointensity as a dating tool in SBG. While other possible sources of error (such as a local field effect) cannot be neglected, we find that the paleointensity dates from 17–18°S are in excellent agreement with all available observational and radiometric data.

Appendix A

[63] The equations required to model structural relaxation in glass have been developed elsewhere, with *DeBolt et al.* [1976] the first to apply them to continuous heating or cooling data. We summarize the mathematical development and the technique below. Refer to Table 4 for a list of symbols used in the text.

[64] As discussed in the main text, structural change, represented by fictive temperature (T_f), is monitored through measurement of heat capacity ($c_p = dH/dT \propto dT_f/dT$). We heat the pristine sample at a known rate, allowing it to relax back into structural equilibrium along a path dependent (in part) upon its prior cooling history. The exact geometry of the resulting heat capacity curve is also related to sample chemistry. To isolate this latter effect, we then cycle the sample through a series of matched cooling and heating runs to calibrate the relaxation response of the glass.

[65] To model the heating curve, we need an expression for structural relaxation in glass that we can use to compute changes in T_f with T ($c_p = dT_f/dT$). Structural relaxation in glass has been shown to be both nonexponential and nonlinear in nature [*Narayanaswamy*, 1971; *Scherer*, 1986]. The nonexponentiality means that the relaxation response of the glass to a step change in temperature cannot be described by a simple exponential with a single relaxation time. The true relaxation response can instead be approximated by summing over a weighted series of exponentials with different relaxation times. It has also been dealt with successfully by use of an empirical equilibrium relaxation function [*Williams and Watts*, 1970]:

$$\phi(t) = \exp\left[-(t/\tau_0)^{\beta}\right], \tag{A1}$$

where t is time. This expression uses a single (temperature-dependent) characteristic relaxation

time, τ_0, modified by the exponent β ($0 < \beta \leq 1$), which is related to the relaxation spectrum width, or the degree of nonexponentiality. If $\beta = 1$, a simple exponential equation is recovered. This function has been used to model relaxation in a variety of silicate melts [*DeBolt et al.*, 1976; *Martens et al.*, 1987; *Wilding et al.*, 2000].

[66] In addition to the nonexponentiality of structural relaxation, a nonlinearity results from viscosity which is both temperature and structure dependent [*Narayanaswamy*, 1971]. This means that even at constant temperature, the relaxation time will change as a nonequilibrium structure relaxes. The relaxation response thus depends on both the direction and magnitude of the temperature change, ΔT. *Narayanaswamy* [1971] has addressed this by letting the relaxation time vary with both temperature and structure (T_f) in a modified form of the Arrhenius equation:

$$\tau_0(T, T_f) = A^{-1} \exp\left[\frac{x\,\Delta H^*}{R\,T} + \frac{(1-x)\Delta H^*}{R\,T_f}\right], \qquad \text{(A2)}$$

where x ($0 \leq x \leq 1$) varies between zero and one and specifies the degree to which τ_0 depends on structure. ΔH^* is the activation enthalpy, R is the gas constant, and A is a constant.

[67] So the response to a single step change in temperature ΔT at t_1 (for $t > t_1$) can be represented as

$$T_f(t) = T_0 + \Delta T\left[1 - \exp\left\{-\left(\int_{t_1}^{t} \frac{dt}{\tau_0}\right)^{\beta}\right\}\right], \qquad \text{(A3)}$$

with τ_0 found as in (A2). The response to a series of m step changes can be taken as the superposition of the individual responses:

$$T_f(t) = T_0 + \sum_{j=1}^{m} \Delta T_j\left[1 - \exp\left\{-\left(\int_{t_j}^{t} \frac{dt}{\tau_0}\right)^{\beta}\right\}\right] \qquad \text{(A4)}$$

If we approximate the instantaneous heating or cooling rate, q, as a series of steps $\Delta T/\Delta t$, then T_f as a function of temperature during continuous cooling or heating can be written as [*DeBolt et al.*, 1976]

$$T_{f,m} = T_o + \sum_{j=1}^{m} \Delta T_j\left[1 - \exp\left\{\left(-\sum_{k=j}^{m} \frac{\Delta T_k}{q_k \tau_{0,k}}\right)^{\beta}\right\}\right], \qquad \text{(A5)}$$

where T_0 is some temperature above the glass transition where the system is in equilibrium. The subscript m is an index indicating the mth temperature step from the beginning of calculations. Note that because of the memory effect, calculations must be carried out starting above T_g. This means that in order to calculate a heating curve, a cooling curve must first be calculated.

[68] We now have a relaxation model with four unknown kinetic parameters (A, ΔH^*, x, and β) that are related to sample composition. The temperature derivative of equation (A5) can be directly compared to the measured heat capacity curve, after the latter has been normalized to zero below T_g and to one above T_g.

[69] Before we can solve for the original cooling rate, we must find the best-fit kinetic parameters for the sample, which is done using the "calibration" relaxation curves with matched cooling and heating rates. A and ΔH^* can be found by solving the Arrhenius equation in a least squares sense using the known values of q and T_g from each calibration curve:

$$-\ln|q| = -\ln A + \frac{\Delta H^*}{RT_g}. \qquad \text{(A6)}$$

A and ΔH^*, along with starting guesses for x and β, are then fed into a fitting routine that models $\Delta T_f/\Delta T$ using equations (A2) and (A5) and solves for the best-fit values of A, ΔH^*, x, and β using all calibration heating curves. The fitting routine is a multidimensional minimization using the downhill simplex method of *Nelder and Mead* [1965]. The routine minimizes the RMS misfit between the measured and modeled curves, plus additional penalties on peak height and location. Once the best-fit kinetic parameters have been found, these values are fixed and the c_p curve from the first heating of the sample is modeled, solving for the unknown quench rate.

Acknowledgments

[70] The authors would like to sincerely thank Gustaf Arrhenius for use of the DSC and for assistance in its calibration and in the initial interpretation of data. Bill Paplawsky was of great help in getting the DSC up and running. Thanks to Jason Steindorf for assistance with many of the paleomagnetic measurements. We would also like to thank Andy Jackson, Mireille Perrin, and one anonymous reviewer for helpful comments on the manuscript. This work

was done with support from NSF grants OCE0095698 and OCE0095342. This is LDEO contribution 6752.

References

Auzende, J.-M., et al. (1996), Recent tectonic, magmatic, and hydrothermal activity on the East Pacific Rise between 17°S and 19°S: Submersible observations, *J. Geophys. Res.*, *101*, 17,995–18,010.

Bergmanis, E. C., J. M. Sinton, K. H. Rubin, J. J. Mahoney, J. Bowles, J. S. Gee, and M. C. Smith (2004), Magma reservoir dynamics and diverse mantle melting at the southern East Pacific Rise, 17°22′S–17°35′S, *Eos Trans. AGU*, *85*(47), Fall Meet. Suppl., Abstract V53A-0611.

Bowles, J., J. Gee, J. A. Hildebrand, and L. Tauxe (2002), Archaeomagnetic intensity results from California and Ecuador: Evaluation of regional data, *Earth Planet. Sci. Lett.*, *203*, 967–981.

Buddington, A. F., and D. H. Lindsley (1964), Iron-titanium oxide minerals and synthetic equivalents, *J. Petrol.*, *5*, 310–357.

Carlut, J., and D. V. Kent (2000), Paleointensity record in zero-age submarine basalt glasses: Testing a new dating technique for recent MORBs, *Earth Planet. Sci. Lett.*, *183*, 389–401.

Carlut, J., M.-H. Cormier, D. V. Kent, K. E. Donnelly, and C. H. Langmuir (2004), Timing of volcanism along the northern East Pacific Rise based on paleointensity experiments on basaltic glasses, *J. Geophys. Res.*, *109*, B04104, doi:10.1029/2003JB002672.

Coe, R. S. (1967), The determination of paleo-intensities of the Earth's magnetic field with emphasis on mechanisms which could cause non-ideal behavior in Thellier's method, *J. Geomagn. Geoelectr.*, *19*(3), 157–179.

Coe, R. S., S. Gromme, and E. A. Mankinen (1978), Geomagnetic paleointensities from radiocarbon-dated lava flows on Hawaii and the question of the Pacific nondipole low, *J. Geophys. Res.*, *83*, 1740–1756.

DeBolt, M. A., A. J. Easateal, P. B. Macedo, and C. T. Moynihan (1976), Analysis of structural relaxation in glass using rate heating data, *J. Am. Ceram. Soc.*, *59*, 16–21.

Dodson, M. H., and E. McClelland-Brown (1980), Magnetic blocking temperatures of single-domain grains during slow cooling, *J. Geophys. Res.*, *85*, 2625–2637.

Efron, B. (1982), *The Jackknife, the Bootstrap and Other Resampling Plans*, 92 pp., Soc. for Ind. and Appl. Math., Bristol, UK.

Fabian, K. (2003), Some additional parameters to estimate domain state from isothermal magnetization measurements, *Earth Planet. Sci. Lett.*, *213*, 337–345.

Fox, J. M. W., and M. J. Aitken (1980), Cooling-rate dependence of thermoremanent magentization, *Nature*, *283*, 462–463.

Gee, J. S., S. C. Cande, J. A. Hildebrand, K. Donnelly, and R. L. Parker (2000), Geomagnetic intensity variations over the past 780 kyr obtained from near-seafloor magnetic anomalies, *Nature*, *408*, 827–832.

Genevey, A., and Y. Gallet (2002), Intensity of the geomagnetic field in western Europe over the past 2000 years: New data from ancient French pottery, *J. Geophys. Res.*, *107*(B11), 2285, doi:10.1029/2001JB000701.

Halgedahl, S. L., R. Day, and M. Fuller (1980), The effect of cooling rate on the intensity of weak-field TRM in single-domain magnetite, *J. Geophys. Res.*, *85*, 3690–3698.

Heller, R., R. T. Merrill, and P. L. McFadden (2002), The variation of intensity of Earth's magnetic field with time, *Phys. Earth Planet. Inter.*, *131*, 237–249.

Jackson, A., A. R. T. Jonkers, and M. R. Walker (2000), Four centuries of geomagnetic secular variation from historical records, *Philos. Trans. R. Soc. London, Ser. A*, *358*, 957–990.

Kent, D. V., and J. Gee (1996), Magnetic alteration of zero-age oceanic basalt, *Geology*, *24*, 703–706.

Kinoshita, H., H. Fujusawa, N. Sakai, H. Sato, and H. Watanabe (1996), Effect of hydrostatic pressure on the thermal conductivity of basalt from Hole 504B, with some reassessment of the shipboard data, *Proc. Ocean Drill. Program Sci. Results*, *148*, 397–400.

Martens, R. M., M. Rosenhauer, H. Büttner, and K. Von Gehlen (1987), Heat capacity and kinetic parameters in the glass transformation interval of diopside, anorthite and albite glass, *Chem. Geol.*, *62*, 49–70.

Naar, D. F., and R. N. Hey (1989), Recent Pacific-Easter-Nazca plate motions, in *Evolution of Mid-Ocean Ridges*, *Geophys. Monogr. Ser.*, vol. 57, edited by J. M. Sinton, pp. 9–30, AGU, Washington, D. C.

Narayanaswamy, O. S. (1971), A model of structural relaxation in glass, *J. Am. Ceram. Soc.*, *54*, 491–498.

Nelder, J. A., and R. Mead (1965), A simplex method for function minimization, *Comput. J.*, *7*, 308–313.

Pick, T., and L. Tauxe (1993), Holocene paleointensities: Thellier experiments on submarine basaltic glass from the East Pacific Rise, *J. Geophys. Res.*, *98*, 17,949–17,964.

Rubin, K. H., M. C. Smith, L. F. Sacks, J. Sinton, and E. Bergmanis (2001), ^{238}U-^{230}Th-^{226}Ra-^{210}Pb constraints on eruption timing for discrete lava flows on the S-EPR, *Eos Trans. AGU*, *82*(47), Fall Meet. Suppl., F1279.

Scherer, G. W. (1986), *Relaxation in Glass and Composites*, 331 pp., John Wiley, New York.

Selkin, P. A., J. S. Gee, L. Tauxe, W. P. Meurer, and A. J. Newell (2000), The effect of remanence anisotropy on paleointensity estimates: A case study from the Archean Stillwater Complex, *Earth Planet. Sci. Lett.*, *183*, 403–416.

Shah, A. K., M. Cormier, W. B. F. Ryan, W. Jin, J. Sinton, E. Bergmanis, J. Carlut, A. Bradley, and D. Yoerger (2003), Episodic dike swarms inferred from near-bottom magnetic anomaly maps at the southern East Pacific Rise, *J. Geophys. Res.*, *108*(B2), 2097, doi:10.1029/2001JB000564.

Sinton, J., E. Bergmanis, K. Rubin, R. Batiza, T. K. P. Gregg, K. Grönvold, K. C. Macdonald, and S. M. White (2002), Volcanic eruptions on mid-ocean ridges: New evidence from the superfast spreading East Pacific Rise, 17°–19°S, *J. Geophys. Res.*, *107*(B6), 2115, doi:10.1029/2000JB000090.

Stacey, F. D., and S. K. Banerjee (1974), *The Physical Principles of Rock Magnetism*, 195 pp., Elsevier, New York.

Tauxe, L., and H. Staudigel (2004), Strength of the geomagnetic field in the Cretaceous Normal Superchron: New data from submarine basaltic glass of the Troodos Ophiolite, *Geochem. Geophys. Geosyst.*, *5*, Q02H06, doi:10.1029/2003GC000635.

Thellier, E., and O. Thellier (1959), Sur l'intensité du champ magnétique terrestre dans le passé historique et géologique, *Ann. Geophys.*, *15*, 285–378.

Tool, A. Q. (1946), Relation between inelastic deformability and thermal expansion of glass in its annealing range, *J. Am. Ceram. Soc.*, *29*, 240–253.

Turcotte, D. L., and G. Schubert (2002), *Geodynamics*, 456 pp., Cambridge Univ. Press, New York.

Vosteen, H.-D., and R. Schellschmidt (2003), Influence of temperature on thermal conductivity, thermal capacity and thermal diffusivity for different types of rock, *Phys. Chem. Earth*, *28*, 499–509.

Wallace, P. J., J. Dufek, A. T. Anderson, and Y. Zhang (2003), Cooling rates of Plinian-fall and pyroclastic-flow deposits in the Bishop Tuff: inferences from water speciation in quartz-hosted glass inclusions, *Bull. Volcanol.*, *65*, 105–123.

Walton, D. (1980), Time-temperature relations in the magnetization of assemblies of single domain grains, *Nature*, *286*, 245–247.

Wilding, M. C., S. L. Webb, and D. B. Dingwell (1995), Evaluation of a relaxation geospeedometer for volcanic glasses, *Chem. Geol.*, *125*, 137–148.

Wilding, M., D. Dingwell, R. Batiza, and L. Wilson (2000), Cooling rates of hyaloclastites: Applications of relaxation geospeedometry to undersea volcanic deposits, *Bull. Volcanol.*, *61*, 527–536.

Williams, G., and D. C. Watts (1970), Non-symmetrical dielectric relaxation behavior arising from a simple empirical decay function, *Trans. Faraday Soc.*, *66*, 80–85.

Yovanovich, M. M. (1996), Simple explicit expressions for calculation of the Heisler-Grober charts, paper presented at ASME National Heat Transfer Conference, Am. Inst. of Aeronaut. and Astronaut., Houston, Tex.

Yu, Y., and L. Tauxe (2005), On the use of magnetic transient hysteresis in paleomagnetism for granulometry, *Geochem. Geophys. Geosyst.*, *6*, Q01H14, doi:10.1029/2004GC000839.

Zhou, W., R. Van der Voo, D. R. Peacor, and Y. Zhang (2000), Variable Ti-content and grain size of titanomagnetite as a function of cooling rate in very young MORB, *Earth Planet. Sci. Lett.*, *179*, 9–20.